UNIVERSITÀ DEGLI STUDI DI PADOVA

Dipartimento di Fisica e Astronomia "Galileo Galilei"

Master Degree in Physics

Final Dissertation

Study of thermal noise in solids out of thermodynamic equilibrium

Thesis supervisor

Prof. Giacomo Ciani

Thesis co-supervisor

Dr. Livia Conti

Candidate

Mirko Menni

Academic Year 2021/2022

Contents

Introduction

Nature is full of tiny random fluctuations, for example, a circuit continuously hosts a background current, a solid body presents imperceptible vibrations and if a body suspended in a liquid is small enough, its motion is erratic. Those of these fluctuations that are related to temperature, that increase with it, are called thermal noise. The behaviour and magnitude of these fluctuations are well understood in thermodynamic equilibrium, while in the wider field of non-equilibrium conditions the experimental results and the related theories are still marginally developed.

Thermal noise provides fundamental limits to the sensitivity of high precision experiments, and while in situations close enough to thermodynamic equilibrium it can be accurately modeled and accounted for, in non-equilibrium conditions we lack the proper tools to predict it appropriately. An example is provided by the interferometric gravitational wave detectors, whose mirrors have a not homogeneous temperature because of the power they absorb from the laser beam. These mirrors contribute to the noise of the interferometric output via their thermal noise-driven mechanical vibrations, the knowledge of which can lead to its reduction via an appropriate design of the experimental setup. Moreover, future detectors will have some elements at cryogenic temperature, pushing them even farther from the approximation of thermodynamic equilibrium. With the aim of investigating how thermal noise may differ from the estimates provided by the equilibrium theory, the RareNoise experiment was performed. It compared the thermal noise-driven mechanical vibrations of a solid sample in equilibrium and also non-equilibrium conditions, with a stable temperature gradient. An important dependence of thermal noise not only on the (average) temperature of a solid but also on its temperature gradient was observed.

In this thesis I describe the upgrade and characterization of a similar experiment that has been recently setup with the aim of confirming and extending RareNoise findings. In particular, investigations on the calibration of the measuring apparatus are performed. Our test sample is an aluminum oscillator consisting of a suspended rod with a cubic mass at one end. Its oscillations in the longitudinal and the transverse normal mode have rms amplitudes of the order of 10 fm and frequencies around 1400 Hz and 300 Hz. We detect them with a quadrature phase differential interferometer, which is based on the functional principle of the Michelson interferometer but it exploits the two perpendicular polarizations to follow the displacement of the sample over distances longer than a quarter-wavelength of the laser.

In chapter 1 we describe thermal noise in thermodynamical equilibrium and its investigation out of equilibrium performed by the RareNoise experiment. Chapter 2 shows our experimental apparatus. In chapter 3 we describe the interferometer and the analysis procedure. Finally, in section 4 experimental results are shown, in which we focus on the calibration of the measuring apparatus.

Chapter 1

Thermal noise

1.1 Theory in thermodynamic equilibrium

Thermal noise is a class of noises in which the fluctuations are connected to the kinetic energy of microscopic constituents, which depends on temperature. Some examples are Brownian motion and Nyquist noise. At first the single phenomena were described with specific treatments [1] [2], then these results received a common description, which was demonstrated with the fluctuation-dissipation theorem (FDT) in 1951, based on quantum mechanical treatment [3]. It describes a linear dissipative system, that is a system that absorbs power proportionally to the square of the applied perturbation, with energy levels densely distributed. The type of the perturbation is left general and it is described by a generalized force that appears as the term V in the hamiltonian

$$H = H_0(q_1, ..., p_1, ...) + V(t)Q(q_1, ..., p_1, ...), \tag{1.1}$$

where H_0 is the hamiltonian without the perturbation. A generalized impedance $Z(\omega)$ is defined as the ratio between the generalized force V and the corresponding response $\dot{Q}$:

$$Z(\omega) = \frac{V(\omega)}{\dot{Q}(\omega)}. \tag{1.2}$$

The FDT, in thermodynamic equilibrium, states that the (one-sided) power spectral density (PSD) (see appendix A) of the generalized force V, associated to thermal noise, considering a PSD referred to a 1-Hz bandwidth, has the following expression:

$$S_{VV}(\omega) = \left(4\frac{\hbar\omega}{e^{\frac{\hbar\omega}{k_B T}} - 1} + 2\hbar\omega \right) \mathrm{Re}[Z(\omega)] \simeq 4k_B T \mathrm{Re}[Z(\omega)], \tag{1.3}$$

with T the temperature of the system. The term $2\hbar\omega\mathrm{Re}[Z(\omega)]$ is the zero point noise fluctuation, or zero point energy, a temperature-independent term which is the only non-vanishing one at the temperature of 0 Kelvin and which provides a frequency-divergent contribution; presently, this term is an open topic and its role and validity are still discussed [4]. Anyway, the description of the experimental results that has been achieved can be carried out with only the first term of (1.3). Furthermore, almost all our experimental evidence is related to frequencies not too high, i.e. with $\hbar\omega \ll k_B T$, and therefore they can be described by the approximation in (1.3), which provides the classical prediction (an exception is thermal radiation, for which such approximation would provide the ultraviolet catastrophe; it will be discussed in section 1.2.3). According to this formula, the microscopic fluctuations of a system in thermodynamic equilibrium are connected to its macroscopic dissipative behavior, which characterizes non-equilibrium situations, in particular the fluctuations are proportional to the real part of the impedance.

V is a stochastic force described by the Langevin equation [5]:

$$V(t + dt) = V(t) + A(V(t), t)dt + D^{1/2}(V(t), t)N(t)dt^{1/2}, \tag{1.4}$$

where $N(t)$ is the unit normal random variable, A is the drift function and D is the diffusion function. V results with null mean and delta-correlated, that is with the time autocorrelation function consisting of a Dirac delta:

$$\Gamma_V(\tau) = \langle V(t+\tau)V(t)\rangle = 2k_BT\mathrm{Re}[Z(\omega)]\delta(\tau), \tag{1.5}$$

where the factor multiplying the dirac delta is in accordance with the $S_{VV}(\omega)$ predicted by the FDT (in the approximated form of (1.3)), following their connection stated by the Wiener-Khinchin theorem (see A.7 in appendix). This delta-function shape of the autocorrelation function means that there is not correlation between the values of the force V in any two distinct instants of time.

Thermal noise acts as a stochastic force driving the internal acoustic modes of a solid. In our experiment this consists of a suspended rod with a mass at one end, acting as a mass-spring system. For such a case, the system is considered as a damped harmonic oscillator on which a force can act, with the consequent dissipation of the oscillator. So the FDT can be applied, and for it that force F is the generalized force V and the displacement x of the oscillator from the equilibrium position is the corresponding Q (see the relations (1.1) and (1.2)) [6]. This means that the generalized impedance results

$$Z(\omega) = \frac{F(\omega)}{\dot{x}(\omega)}. \tag{1.6}$$

A first way in which the oscillator can be modeled is with a velocity damping (VD), i.e. with a frictional force $F_{friction} = -f\dot{x}$. Then the equation of motion is given adding the Hooke's law restoring force and an additional force due to thermal noise F:

$$m\ddot{x}(t) = -kx(t) - f\dot{x}(t) + F(t), \tag{1.7}$$

where m is the mass of the oscillator and k is the spring constant.

The equation in frequency domain is

$$x(\omega)\left(-m\omega^2 + k + i\omega f\right) = F(\omega), \tag{1.8}$$

and x results:

$$x(\omega) = \frac{F(\omega)}{-m\omega^2 + k + i\omega f} \equiv H(\omega)F(\omega). \tag{1.9}$$

Then the PSD of x can be expressed as function of the PSD of F:

$$S_{xx,VD}(\omega) = |H(\omega)|^2 S_{FF}(\omega) = \frac{S_{FF}(\omega)}{\left(m\omega^2 - k\right)^2 + f^2\omega^2}. \tag{1.10}$$

The real part of the generalized impedance can be calculated with the equation of motion passing to the frequency domain:

$$R(\omega) = Re[Z(\omega)] = Re\left[\frac{F}{\dot{x}}\right] = Re\left[\frac{\left(-m\omega^2 + k + i\omega f\right)x(\omega)}{i\omega x(\omega)}\right] = Re\left[i\left(m\omega - \frac{k}{\omega}\right) + f\right] = f. \tag{1.11}$$

Now, from (1.10) exploiting (1.3) and (1.11), you obtain:

$$S_{xx,VD}(\omega) = \frac{4k_BTf}{\left(m\omega^2 - k\right)^2 + f^2\omega^2} = \frac{4k_BT\gamma/m}{\left(\omega^2 - \omega_0^2\right)^2 + \gamma^2\omega^2}, \tag{1.12}$$

where in the last passage $k = m\omega_0^2$, with ω_0 the resonance frequency, and $f = m\gamma$, where γ is the full-width-at-half-maximum (FWHM).

This model with a velocity damping is not properly correct for a low-loss oscillator, that is our case [6]. In general it is described using the model of internal damping (ID), with the restoring force following an extension of the Hooke's law with a complex spring constant, which can be approximated

by $F \simeq -k(1 + i\phi(\omega))x$. The damping comes from a delay of the response of the oscillator respect to the restoring force, and a fraction $2\pi\phi(\omega)$ of the energy of the oscillation is dissipated in each cycle. In various materials $\phi(\omega)$ results approximately constant over a large band of frequencies. Through the same calculations made for the velocity damping case you get:

$$S_{xx,ID}(\omega) = \frac{4k_BTk\phi(\omega)}{\omega\left[(m\omega^2 - k)^2 + k^2\phi(\omega)^2\right]} = \frac{4k_BT\omega_0^2\phi(\omega)}{m\omega\left[\left(\omega^2 - \omega_0^2\right)^2 + \omega_0^4\phi(\omega)^2\right]}. \tag{1.13}$$

The sharpness of the resonance is customary denoted by the quality factor $Q = \frac{\omega_0}{\Delta\omega}$, with ω_0 the resonance frequency and $\Delta\omega$ the FWHM. For the case of velocity damping $Q = \omega_0/\gamma$ while for internal damping $Q = 1/\phi(\omega_0)$. For low loss oscillators the PSD of the displacement x is sharply peaked around the resonance frequency ω_0 [6]. Examples for the PSDs provided by the two models are shown in figure 1.1.

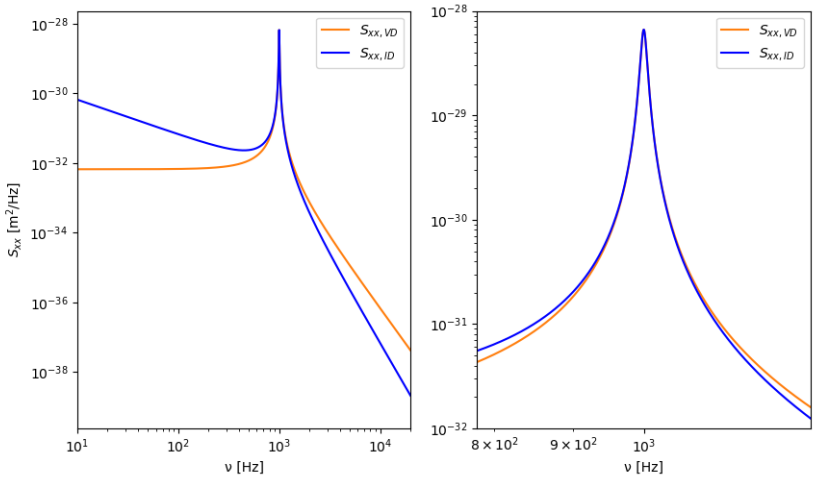

Figure 1.1: Example PSDs for the two cases of velocity damping (VD) and internal damping with ϕ constant (ID). The right plot is zoomed in frequency. $T = 298$K, $m = 100$g, $f_0 = 1000$Hz, $Q = 100$.

In both the cases, with velocity damping and internal damping, the integral of the PSD in frequency domain (see A.5) provides the same prediction for the average square displacement of the oscillator [6]:

$$\langle x_{Th}^2 \rangle = \int_0^{+\infty} S_{xx} d\nu = \frac{k_BT}{k}. \tag{1.14}$$

The result is consistent with the equipartition theorem, which states that each quadratic contribution of a degree of freedom to the energy, and in particular the potential energy of the oscillator $\frac{1}{2}kx^2$, has a mean energy of $\frac{1}{2}k_BT$.

1.2 Experimental overview in thermodynamic equilibrium

Thermal noise is one of the fundamental limits of high sensitivity measurements. For this reason it is also a very well studied phenomenon in various experimental conditions. In the following, examples of measurements of thermal noise manifesting in different kind of phenomena are described.

1.2.1 Brownian motion

With the invention of microscope around the beginning of the 17th century, a lot of new very small organisms were observed. Brown's studies were particularly important [1], in 1828 he described very wide and accurate observations: very small bodies, such as pollen, suspended in a still liquid and observed with microscope, show erratic movements, without apparent cause or explanation. Moreover,

these movements are observable not only with bodies belonging to the living reigns of nature, which could manifest a certain form of life, but even with minerals. In 1905 Einstein proposed an explanation based on the atomic theory and on the equipartition theorem, providing quantitative predictions, which were verified by Perrin in 1908. On the one hand this led to the end of the debate on the existence of atoms, on the other it was the first quantitative description of noise, which was followed by many other studies in many fields in the following years and decades.

A small body suspended in a stationary liquid, neglecting the gravitational force, follows the equation of motion given by

$$m\ddot{\vec{x}} = -f\dot{\vec{x}} + F_{th}, \tag{1.15}$$

where for the case of a sphere $f = 6\pi\mu a$ depending on the viscosity μ and the radius a of the spherical body and F_{th} is the thermal noise force, which can be described by the FDT: the real part of the generalized impedance results $\mathrm{Re}[Z] = f$ (with calculations similar to those that leads to (1.11)), getting the PSD for the random force:

$$S_{F_{th},F_{th}}(\omega) = 4k_BTf. \tag{1.16}$$

So, the body is accelerated by the thermal noise force F_{th}, which is random and with a null mean, and is dampened by the friction of the liquid $-f\dot{\vec{x}}$ (given by the Stokes law), so that the mean kinetic energy for each spatial direction is that predicted by the equipartition theorem $\frac{1}{2}k_BT$, while the direction of the velocity is random. Based on these premises, the motion can be statistically described; in particular, for each spatial dimension x_i, the mean distance reached by the body after a time t results [1]

$$\overline{\Delta x_i} = \sqrt{\frac{k_BT}{3\pi\mu a}t}. \tag{1.17}$$

This means that a random null mean force acting on the body causes a mean displacement increasing with the square root of the time. In figure 1.2 there are three examples of measured paths.

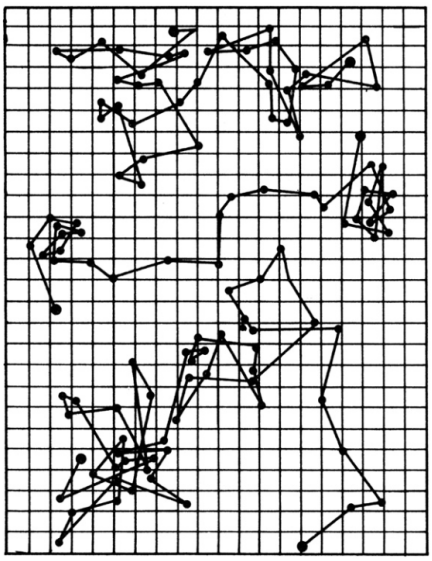

Figure 1.2: Brownian motion displacements of three particles measured by Perrin. For each path the position of the body is marked at regular intervals of time and then the various positions are joint with a straight line. [7]

1.2.2 Electronic thermal noise

The field of electronics has been one of the first sources of studies on noise and one of the most prominent ones [1]. In the Schottky's paper of 1918 both thermal noise and shot noise were described for the first time. A subsequent important and wide experimental study was provided by Johnson in 1928 [8]. He measured electronic thermal noise as the mean square electromotive force that develops

between the ends of a conductor in equilibrium, which is due to the thermal agitation of the charges. He observed that such noise is proportional to the temperature and the resistance of the conductor. Moreover, the proportionality constant is the same for different conductors, with different sizes, shapes and materials. In figure 1.3 the experimental data are plotted.

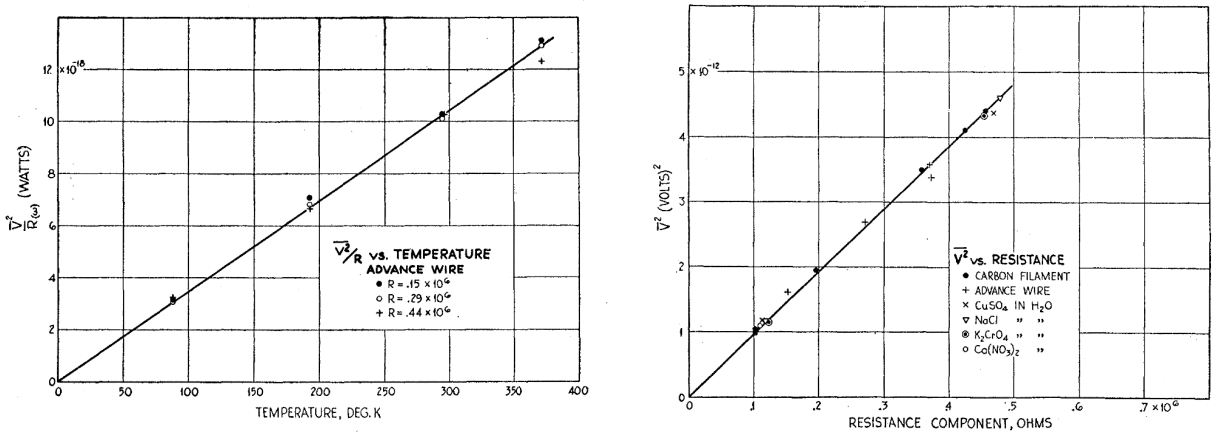

Figure 1.3: Experimental data provided by Johnson showing the proportionality of mean square voltage fluctuations respect to temperature (on the left) and to resistance (on the right). The data comes from different conductors, as indicated in the legend. [8]

In the paper following the Jonsons's one on the same publication, Nyquist provided a theoretical derivation of the phenomenon, in which the thermal agitation of the charges of the conductor causing thermal noise was described exploiting the equipartition theorem and the second principle of thermodynamics, derivation which was in accordance with the Johnson's measures [2]. The PSD of the electromotive force V between the ends of a conductor due to thermal noise (in the classical case) is given by

$$S_{VV}(\omega) = 4k_B T R(\omega). \tag{1.18}$$

We stress that the proportionality of the PSD of the electromotive force respect to R, valid for the various types of conductor, agrees with the second principle of thermodynamics. Indeed in this way, for a circuit with homogeneous temperature, the noise power that a circuital element gives to the rest of the circuit, $P_{e->c}$, is equal to the noise power that the element absorbs from the noise energy provided to the circuit by the other elements, $P_{c->e}$; and this makes the various elements of a circuit remain at the same temperature. In particular, the first power, per unit frequency, results

$$P_{e->c} = S_{II,e->c}(\omega) R_c(\omega) = \frac{S_{VV,e}(\omega)}{|Z_{tot}(\omega)|^2} R_c(\omega) = 4k_B T \frac{R_e(\omega) R_c(\omega)}{|Z_{tot}(\omega)|^2}, \tag{1.19}$$

while the second power results

$$P_{c->e} = S_{II,c->e}(\omega) R_c(\omega) = \frac{S_{VV,c}(\omega)}{|Z_{tot}(\omega)|^2} R_e(\omega) = 4k_B T \frac{R_c(\omega) R_e(\omega)}{|Z_{tot}(\omega)|^2} \equiv P_{e->c}, \tag{1.20}$$

where $S_{II,i->j}$ is the PSD of the thermal noise current provided by the part i of the circuit to the part j (with i and j are e for the element and c for the rest of the circuit), $Z_{tot}(\nu) = R_e + R_c + i(\chi_e + \chi_c)$ is the equivalent total impedance of the circuit seen from the considered element, R_i and χ_i are the Thévenin-equivalent resistance and reactance of the element or of the rest of the circuit and in the final passages the formula (1.18) is used.

1.2.3 Thermal radiation

In their article of 1951 [3], Callen and Welton derived the fluctuation dissipation theorem and then they applied it to different situations. One of them was thermal radiation. They considered an electric

dipole moment of charge e and displacement x, with one charge fixed and the other one oscillating, so that

$$P \equiv ex = P_0 \sin \omega t, \tag{1.21}$$

with the related dissipative force due to electric dipole radiation

$$F_d = -\frac{2e^2}{3c^3}\frac{d^3x}{dt^3}. \tag{1.22}$$

The equation of motion of this charge is

$$m\frac{d^2x}{dt^2} = -m\omega_0^2 x - F_d + F, \tag{1.23}$$

where ω_0 is the natural frequency associated with the intra-dipole binding force and F is the applied force. Inserting (1.21) and (1.22) in (1.23) you get

$$F = \frac{mP_0}{e}(\omega_0^2 - \omega^2)\sin \omega t + \frac{2e\omega^3 P_0}{3c^3}\cos \omega t. \tag{1.24}$$

The real part of the generalized impedance is given by the ratio between the in-phase components of F and $\frac{dx}{dt} = \frac{\omega P_0}{e}\cos \omega t$:

$$R(\omega) = \frac{\frac{2e\omega^3 P_0}{3c^3}}{\frac{\omega P_0}{e}} = \frac{2e^2}{3c^3}\omega^2. \tag{1.25}$$

The FDT provides the PSD of a random force acting on the charge and associated to an electric field, $F_{th,x} = eE_{th,x}$. Considering all the three spatial dimension contributions and deriving the energy density associated to the electric field, you get the energy density per unit frequency ν [3]:

$$u_\nu = \frac{8\pi\nu^2}{c^3}\frac{h\nu}{e^{\frac{h\nu}{k_B T}} - 1}. \tag{1.26}$$

This energy density is that due to the Planck radiation law in condition of thermodynamic equilibrium. The Planck radiation law, expressed as the power per unit frequency per unit volume emitted by the volume of a body, results

$$\rho_{P,em}(\nu) = \alpha\frac{8\pi\nu^2}{c^2}\frac{h\nu}{e^{\frac{h\nu}{k_B T}} - 1} = \alpha n^2 F(T,\nu), \tag{1.27}$$

with α the radiation attenuation coefficient and n the refractive index. This formula results in accordance with the second principle of thermodynamics. Beside a term depending only on T, ν and c (the speed of light in the medium), $\rho_{P,em}(\nu)$ is proportional only to the attenuation coefficient; more precisely, the factor depending on the medium is only αn^2. Differently, if there was an additional factor depending on the material, at a given temperature, one material would be more able to emit power than to absorb it from the other bodies, and thus at thermodynamic equilibrium a body of a certain material would reach a temperature lower than that reached by a second body of an other material, in contrast with the second principle of thermodynamics.

The thought that bodies tend to reach a common temperature comes naturally and the physical studies have confirmed the second principle of thermodynamics in many cases; anyway, in order for it to be possible, various single phenomena have to behave in an adequate way. The density of emitted power has to be proportional to αn^2, without any other dependence on the material. Moreover, as we stressed in the previous section 1.2.2, the power spectral density of the electromotive force due to thermal noise has to be proportional to $R(\nu)$, without other dependence on the material or the shape. Thermal noise does not care about material, but it follows the second principle of thermodynamics.

1.2.4 Torsion balance

Torsion balance is a high-sensitivity measuring instrument used to measure very small forces, so that thermal noise results to be an important factor to be considered. Torsion balance essentially consists of a vertical wire attached at the top end and to which a torque can be provided via an apposite apparatus (see as example figure 1.5). The wire reacts to the torsion with a restoring torque that, in the elastic limit, is proportional to the displacement from the equilibrium angle; so it is used to infer very small forces acting on the apparatus by measuring the deflection angles.

A hindrance to these measurements is thermal noise, which excites the torsion balance. The system follows the equation of motion of a damped torsion pendulum, and in modern experiments the velocity damping, an external one, is negligible respect to the internal damping [9]:

$$I\ddot{\theta} + k(1 + i\phi)\theta = \tau(t), \tag{1.28}$$

where I is the moment of inertia, k is the torsional spring constant, ϕ is the loss angle of the spring, θ is the deflection angle of the balance from the equilibrium one and τ is the external torque. Then, through the fluctuation-dissipation theorem you find the PSD of the torque and of the angle due to thermal noise:

$$S_{\tau\tau}(\omega) = 4k_BTR(\omega) = \frac{4k_BTk\phi}{\omega} \tag{1.29}$$

$$S_{\theta\theta} = \frac{4k_BTk\phi}{\omega\left[(I\omega^2 - k)^2 + k^2\phi^2\right]}. \tag{1.30}$$

In figure 1.4 there is the measured PSD of the noise of an example torsion balance. The blue line is the theoretical prediction for the noise of thermal origin and below and around the resonance frequency it is in accordance with the data, which means the sensitivity of the measurement reaches the thermal noise limit.

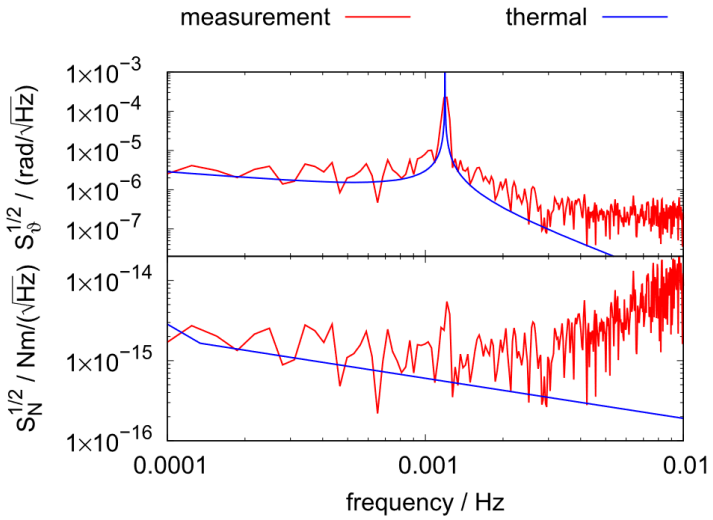

Figure 1.4: Measured noise and theoretical thermal noise of an example torsional oscillator, with k=774pN m rad^{-1}. The top plot shows the PSD of the torsional angle θ, while the bottom plot that of the torque. [9]

The limit provided by thermal noise is usually overcome with a long enough measurement time. Let's consider the following experiment, in which a torsion balance is used to measure radiation pressure with a force at the femto-Newton level [10]. The experimental apparatus is shown in figure 1.5. The oscillator is a gram-sized torsion balance consisting of a coated glass plate suspended by the torsion wire. One end of the plate is hit by a laser beam ("laser 2") that then is reflected, providing a force that twists the torsion balance. An other laser beam is reflected by the centre of the plate and its angle is measured, in order to measure the torsional angle of the plate. The feedback electrodes are

used to influence the dynamics of the oscillator to have a velocity damping behavior. The apparatus is in a high vacuum (10^{-7} mbar) environment, it is surrounded by a heat bath that stabilizes the temperature and it is mounted over an active vibration isolation system.

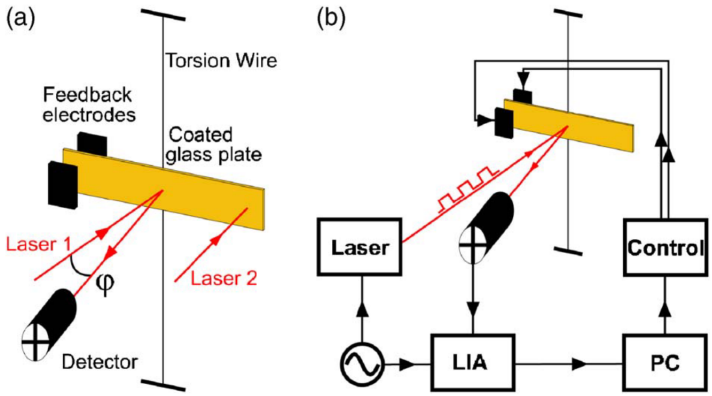

Figure 1.5: (a) The plate is a gold-coated glass plate 50x10x0.15mm in size with a mass of $\sim$ 0.2g and with the arm length, i.e. the distance between the wire and the end of the plate where laser 2 is reflected, is L=0.02m. The torsion wire is a 15cm long tungsten wire, 25 μm in diameter. The pendulum natural frequency is 0.36 Hz with a quality factor $Q \approx 2300$. Laser 2 provides to the balance the force to be measured. Laser 1 is an amplitude-modulated laser beam (100kHz) used to measure the angle of the balance and of which the detected signal is demodulated by a lock-in amplifier (LIA) and used to provide a feedback for the control of the dynamics of the balance, carried out with the two feedback electrodes placed at one end of the plate (see (b)). The reached sensitivity is of $\sim$20 nrad/V and the oscillator angle is measured with an accuracy of $\sim$2 nrad/$\sqrt{Hz}$. [10]

For frequencies much lower than the resonance frequency f_0=0.36 Hz, the PSD of the torque results [10]

$$S_{\tau\tau}(\omega \ll \omega_0) = 4k_B T f, \tag{1.31}$$

where f is the coefficient of the frictional torque $\tau_{friction} = -f\dot{\theta}$. A laser beam modulated at 30 mHz is sent on the end of the arm of the balance (laser 2 in figure 1.5) applying a sinusoidal force $F = \frac{2P}{c}$, with P the radiation power, with a peak-to-peak amplitude of $\sim$ 660 fN. Such force applied to the torsion balance is detectable by the apparatus if it is higher than the minimal detectable force given by

$$F_{min} \geq \frac{\sqrt{S_{\tau\tau}(\omega \ll \omega_0)\Delta f}}{L} = \frac{\sqrt{4k_B T f \tau^{-1}}}{L}, \tag{1.32}$$

where L is the arm length of the torsion balance and Δf is the bandwidth of the detected signal, equal to the inverse of the measurement time τ, which can be increased to reduce F_{min}, so increasing the sensibility of the measuring apparatus. In figure 1.6 the red line shows a measured PSD of the force applied to the balance. For frequencies not too close to 0 Hz, the data follow a background level of $\sim 100 fN/\sqrt{mHz}$ very closed to the limit value provided by thermal noise of $\frac{\sqrt{S_{\tau\tau}(\omega \ll \omega_0)}}{L} = 91.5 fN/\sqrt{mHz}$; and at 30 mHz the very small radiation pressure force is clearly observable.

1.3 Non-equilibrium thermal noise in interferometric GW detectors

In certain high precision experiments thermal noise constitutes a fundamental limit to their sensitivity. Examples are the resonant-mass gravitational waves (GW) detectors and the interferometric GW detectors [6]. The latter is based on a Michelson interferometer: when a GW reaches the earth it stretch and shrink differentially and alternatively the two perpendicular arms of the interferometer hence causing a change in the iterference pattern of the recombining beams. Usually, there is no anticipation of the arrival of a GW, so the detectors take data continuously waiting for a strong enough GW event. In order to detect it, the noise floor has to be low enough. [11]

In figure 1.7 the sensitivity limit estimated for the interferometric detector Advanced VIRGO is plotted, as the sum of contributions coming from various sources of noise. In the low and middle fre-

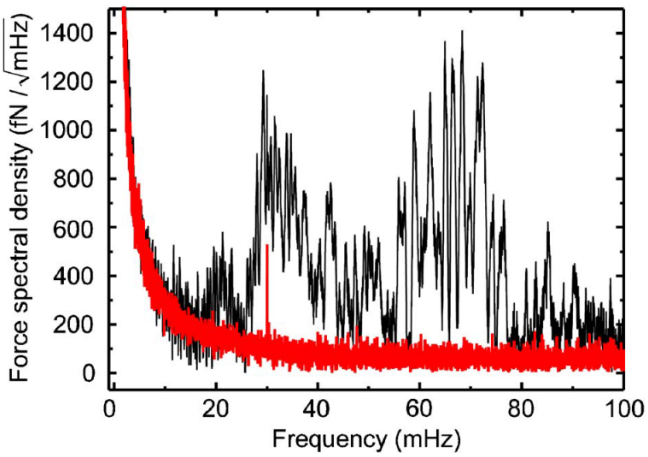

Figure 1.6: The red graph is the high-sensitivity light measurement with the detected force at 30 mHz. The black graph is a measurement under a seismic disturbance, plotted for comparison. [10]

quencies the major contributes that limit the sensitivity are thermal noises, present in the suspensions and in the coatings of the mirrors of the optical system (blue and red lines).

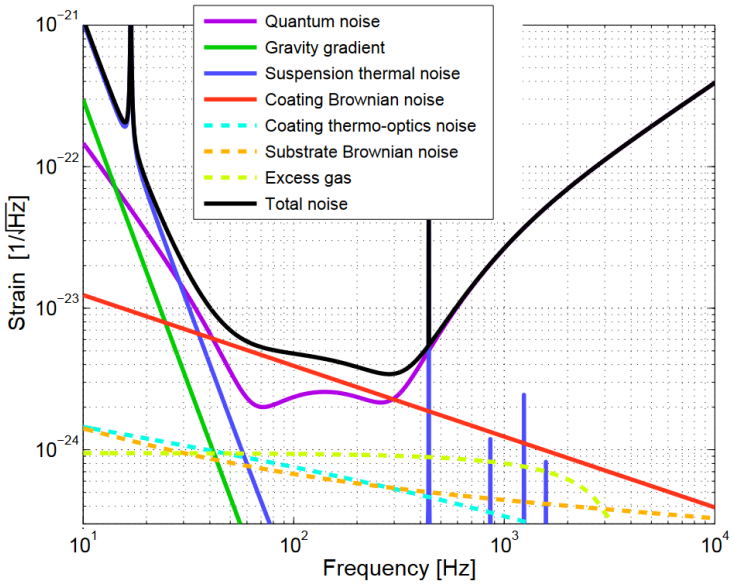

Figure 1.7: Sensitivity limit estimated for Advanced VIRGO experiment. [12]

Thermal noise is evaluated by models in thermodynamic equilibrium and its reduction is performed by lowering the temperature. Anyway, the equilibrium condition is not well justified [11]. The mirrors absorb power from the incident laser and so they reach a higher temperature, while along the mirrors and their suspension fibers the consequent temperature gradient is established. The instrument is further pushed out of equilibrium by the thermal compensation technique, that aims to reduce the mirror thermal lensing due to a not uniform absorption of power from the laser by the mirror; furthermore, additional heat is provided to the mirrors in order to deform them getting the desired radius of curvature. So, there is the requirement to evaluate the validity of the equilibrium description and to find how it differs from the non-equilibrium case; if this difference resulted important, the non-equilibrium description could be used to improve the design of the detector (to obtain a noise floor lower, more stationary and more Gaussian) and the analysis procedure.

For the description of physical systems not in thermodynamic equilibrium various results valid in certain classes of phenomena have been reached, but a general theory is still lacking [11] [13]. Most

of the experiments for non-equilibrium theory involve small-scale systems, because their small masses make thermal noise effects more evident. Anyway, recently certain experiments considered large-scale systems; one of them is described in the following section.

1.4 The RareNoise experiment

The RareNoise experiment was developed to address the question described in the previous section about non-equilibrium thermal noise in GW detectors [11]. It studies the noise vibrations of low-loss mechanical oscillators in non-equilibrium steady state, that is with a stable temperature gradient, in situations similar to those present in the GW interferometers because of the substrates and the coatings of the mirrors and their suspension fibers. The vibrations are measured for a monolithic aluminum sample consisting of a rod fixed at one end and with a cubic load mass at the other end (see figure 1.8). The piece is made in the aluminum alloy Al5056, the same as most of the the GW bar detectors such as AURIGA: this material was chosen because of its low loss properties. The studied oscillations are the first longitudinal mode, with the frequency of about 1420 Hz, and the first transverse flexural mode, at about 320 Hz (see figure 1.8).

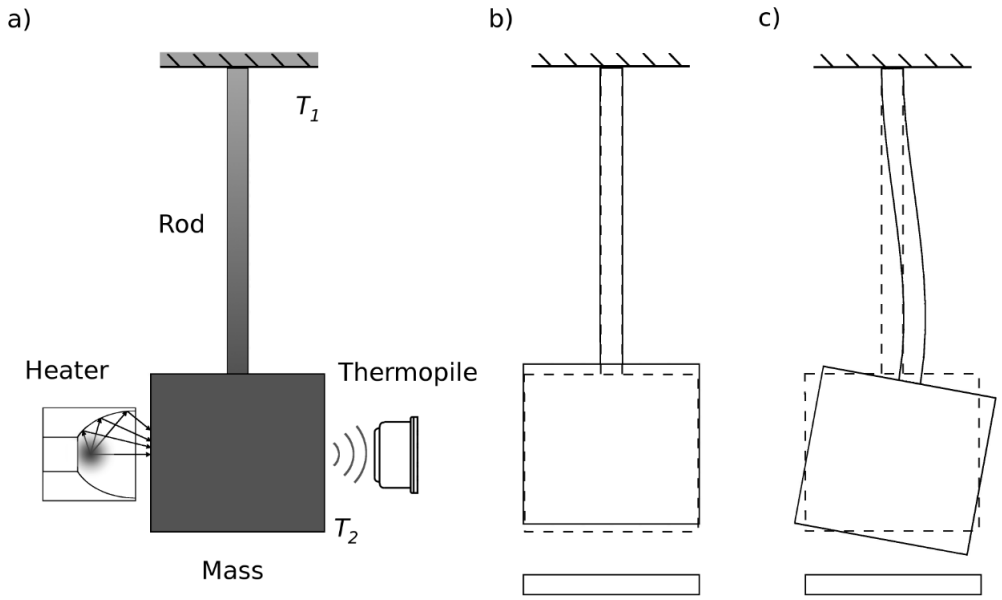

Figure 1.8: Schematic drawing of the oscillator (a) and of its longitudinal (b) and transverse (c) acoustic modes of vibration. In (a) the infrared radiation heater of the cubic mass and the thermopile are present, while in (b) and (c) in the bottom the aluminum plate making up the capacitor is visible. [14]

An aluminum plate is placed below the surface of the load mass at the distance of $60 \div 80$ μm creating a plane capacitor with the surface of the load mass. The noise vibrations of the oscillator change the distance between the two surfaces of the capacitor changing its capacitance. The capacitor is kept at constant charge and the developed voltage is hence amplified and measured, so that from the measured voltage you can estimate the changes of the capacitance and so the noise vibrations of the oscillator. The low noise amplifier connected to the capacitor allows to reach the sensitivity for the displacement of the longitudinal mode of few 10^{-15} m $\mathrm{Hz}^{-1/2}$ [11].

In order to reduce mechanical noise in the setup, the oscillator is suspended by mechanical filters. An active one is provided by an optical table that supports all the apparatus. Moreover, the oscillator is suspended by a cascade of 4 passive mechanical filters effective in all the directions. The oscillator and the passive mechanical filters are held in vacuum by an ion pump, which is vibration free, reaching pressures below 10^{-5}mbar. [15]

In order to control the temperature, the fixed end of the rod of the oscillator can be cooled and

controlled with a Peltier cell, while the load mass can be heated by the radiation of an infrared thermal source (see figure 1.8 or 1.9, in which there's a photo of the oscillator). Being non-contacting, the radiative heating doesn't add external losses to the oscillator. The same can be said for the thermopile, i.e. a non-touching sensor, that measures the temperature of the load mass. With this tools a temperature gradient between the two ends of the oscillator can be established.

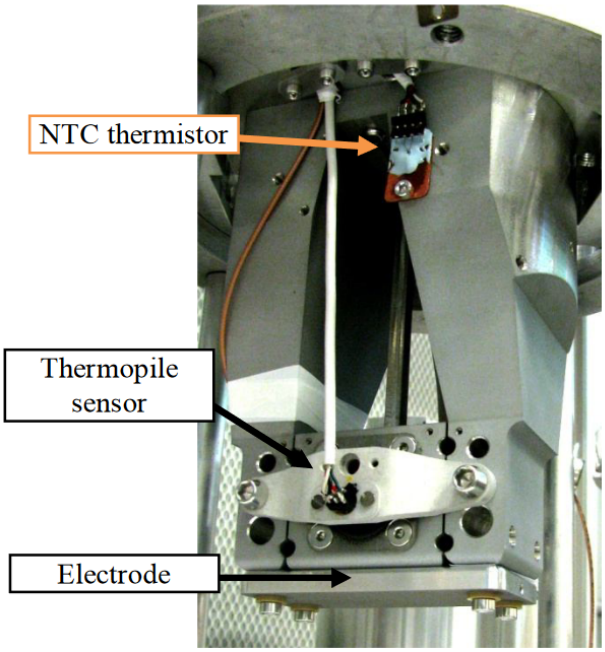

Figure 1.9: Photo of the oscillator, placed between two protrusions that support the aluminum plate ("electrode") forming a capacitor with the cubic mass of the oscillator. The thermopile and the thermistor measuring respectively the temperature of the cubic mass and of the upper end of the oscillator are also visible. [15]

The output of the amplifier can be calibrated in terms of capacitor displacement, hence mode vibrations near its resonance. In the PSD of the output potential, the peaks due to the first transverse and longitudinal acoustic modes of vibration are observable and they are fitted by the Lorentzian curve

$$y(\nu) = y_0 + \frac{2}{\pi} A \frac{w}{4(\nu - \nu_0)^2 + w^2}, \tag{1.33}$$

where y_0 represents the noise level out of the resonance, ν_0 is the resonance frequency, A is the area of the peak, w is the full width at half maximum. This formula can be used because it is a good approximation of (1.12)[1] In figure 1.10 there is an example peak due to the longitudinal vibration fitted by the Lorentzian. From this calibration (for the longitudinal mode) by measuring the area A one can obtain an estimate of the mean square displacement of the lower surface of the mass $\langle x_l^2 \rangle$. In thermodynamic equilibrium, as shown in section 1.1, according to the equipartition theorem you have:

$$\langle x_l^2 \rangle = \frac{k_B T}{k} = \frac{k_B T}{m_l \omega_l^2}, \tag{1.34}$$

where m_l is the mass of the longitudinal mode and ω_l its angular frequency. From this relation, the equilibrium temperature T can be estimated. For non-equilibrium states one can use this same expression to define an effective temperature T_{eff} [14]:

$$T_{eff} = \frac{m_l \omega_l^2 \langle x_l^2 \rangle}{k_B}. \tag{1.35}$$

[1] A part for a factor constant in frequency, the formula (1.12) presents the term $\frac{\gamma}{(\omega^2-\omega_0^2)^2+\gamma^2\omega^2}$, which multiplied by $2\pi\omega_0^2$ provides a function f_1 equivalent in the resonance frequency to the term $f_2 = \frac{w}{4(\nu-\nu_0)^2+w^2}$ in formula (1.33), considering $\omega = 2\pi\nu$, $\omega_0 = 2\pi\nu_0$ and $\gamma = 2\pi w$. Near the resonance, f_1 is approximable to f_2; for instance, at $\omega = \omega_0 \pm 6\frac{\gamma}{2}$ the relative difference is of 0.3% with $Q = \frac{\omega_0}{\Delta\omega} = 10^3$, while it is 0.03% with $Q = 10^4$, and it decreases closer to the resonance frequency.

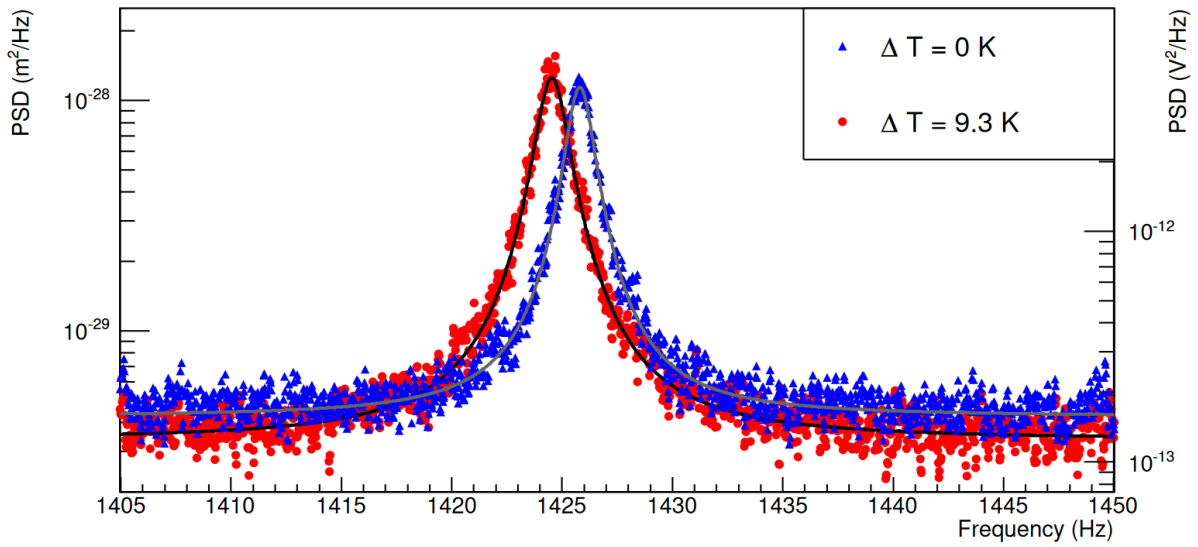

Figure 1.10: example PSDs of the measured voltage around the longitudinal peak, in the cases of equilibrium and of non-equilibrium with the temperatures at the ends of the rod differing of $\Delta T = 9.3$K. The left y axis shows the conversion of the measured potential to the displacement of the mass of the oscillator due to the longitudinal mode of vibration. The data are fitted by a Lorentzian function, from which the effective temperatures results $T_{eff,EQ} = [319 \pm 5(\text{stat.}) \pm 18(\text{syst.})]$ K and $T_{eff,NEQ} = [402 \pm 6(\text{stat.}) \pm 18(\text{syst.})]$ K, respectively for the equilibrium and non-equilibrium case. [14]

In figure 1.11 the measured effective temperatures from the analysis of the longitudinal mode are plotted in function of the average temperature of the oscillator T_{avg}, that in equilibrium is the temperature of the oscillator measured by thermometers while in non-equilibrium is the mean of the temperatures at the two ends of the oscillator. The red line is a linear fit of the equilibrium estimates; its slope results $1.156 \pm 0.001(\text{stat.}) \pm 0.06(\text{syst.})$, that is near the expected unitary value. The mean of the T_{eff} in equilibrium is $T_{EQ} = 338 \pm 12$ (stat.) ± 18 (syst.), which agrees with the measured mean temperature within two standard deviations [14]. Note that these results are achieved without free parameters.

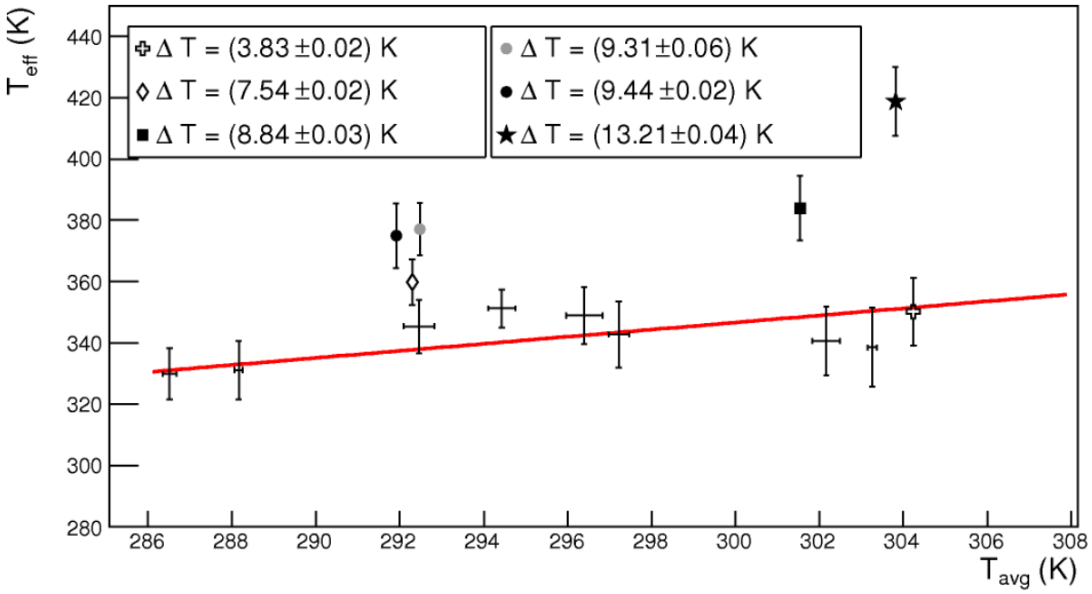

Figure 1.11: Experimental estimates of T_{eff} in equilibrium and non-equilibrium conditions. The red line is the linear fit of the equilibrium estimates. The x axis is the average temperature between the two ends of the oscillator. [14]

To better evaluate the role of the thermal gradient, for both the longitudinal and transverse modes, in figure 1.12 the ratio $R_{NEQ/EQ}$ between the the effective temperature estimated in non-equilibrium and the mean equilibrium effective temperature T_{EQ} is plotted. On the x axis there is the difference of the temperatures measured at the ends of the oscillator ΔT divided by the mean temperature T_{avg}. The estimates of T_{eff} shows the trend to increase with ΔT, with a dependence higher than that on T_{avg} in the equilibrium case. For example, for the longitudinal estimate with the higher $\Delta T/T_{avg}$, a 4% relative temperature difference increases the equilibrium T_{eff} by 20% (i.e. clearly above the T_{eff} of the equilibrium case at the maximum temperature of this non-equilibrium case). This high dependence on ΔT for the transverse case is even higher: a 4% relative temperature difference increases the equilibrium T_{eff} by 200%.

In parallel a numerical experiment using a one dimensional chain of oscillators was performed [14]; the results for the longitudinal mode are the black points in figure 1.12. A theoretical model was elaborated too [14], of which the black line in figure 1.12 is the fit of the points coming from the numerical experiment.

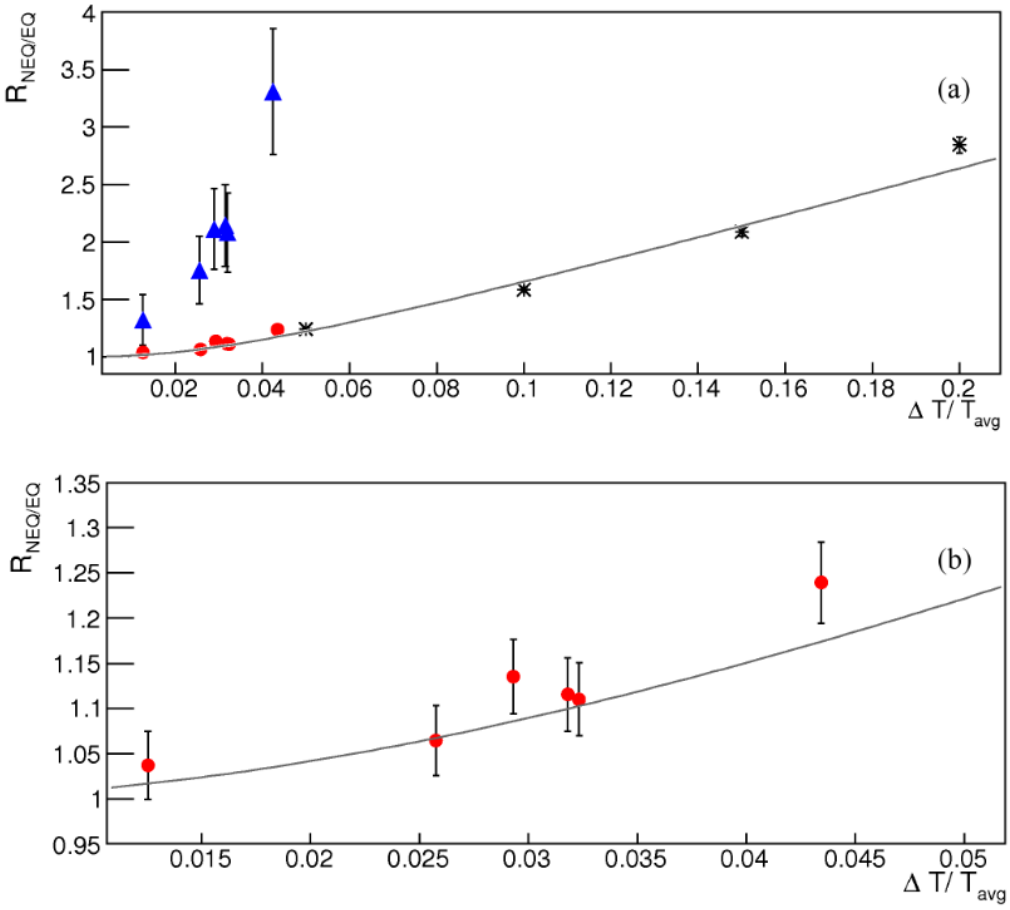

Figure 1.12: The ratio $R_{NEQ,EQ}$ is plotted in function of the relative temperature difference, i.e. the temperature difference between the two ends of the oscillator normalized by the average temperature. The red points comes from the longitudinal mode while the red ones from the transverse mode. The black points come from the numerical experiment while the black line is the fit of the points of the numerical experiment based on the theoretical model. The bottom graph shows only the red points of the top graph. [14]

These results show that the mechanical thermal noise of a solid in a non-equilibrium steady state is not determined only by its average temperature following the equilibrium relation, but the noise is importantly increased by the temperature gradient. The equipartition theorem ceases to be valid, because the longitudinal and the transverse modes of vibration have different T_{eff}, i.e. the energy is not equally divided in the modes, and the energy of the longitudinal mode becomes higher than $\frac{1}{2}k_BT$. This suggests that GW detectors can not be considered as equilibrium system for the estimation of

their noises. Anyway, further investigations on the magnitude of non-equilibrium noise are needed, to better estimate the dependence on the temperature gradient and also to explore other temperature ranges and materials. These measurements have been continued with a different readout, as we will describe in the following chapters.

Chapter 2

The experimental apparatus

The RareNoise experiment, described in the previous section 1.4, provided measurements of thermal noise in non-equilibrium steady states which showed an excess of thermal noise with respect to that estimable by a simple extension of the fluctuation-dissipation theorem. This experiment has continued and in this thesis we describe its current situation. The estimates provided by the RareNoise experiment were affected by a systematic error of about 5% in equilibrium and about 7% out of equilibrium. This was mainly connected to the capacitive readout, in particular because of the uncertainty in the measurements of the capacitance at the amplifier input, the estimate of the oscillator mass, the calibration error in the temperature difference and the error in the thermal expansion. With the aim of overcoming these limits, for this new experiment the readout of the oscillator vibrations was changed: instead of capacitor, we have implemented a phase quadrature differential interferometer and the bottom surface of the cuboid mass constitutes one of the mirrors of this scheme. The advantage of this scheme is that its calibration is independent on the thermal expansion and that it allows to study larger effects by setting up larger thermal differences. In this chapter we describe the whole experimental apparatus and in chapter 3 we focus on the readout.

The latter is composed by the oscillating sample excited by thermal noise that is suspended by mechanical filters, it is placed in a vacuum chamber and it is equipped with a heater. The oscillator is connected to the interferometer, a quadrature phase differential one, endowed with its acquisition system. Except the latter, all the rest is placed on an optical table. An overall photo is reported in figure 2.1.

2.1 The oscillator

We want to measure the thermal noise of the first longitudinal mode of a solid piece, that is a monolithic aluminum (the alloy Al5056) block constituted by a square cross section rod with a cubic mass at one end and hung at the other one (see figure 2.2). In the first longitudinal mode (resonating at about 1.4kHz) we can schematize the piece as a spring-mass system with the cuboid mass acting as the mass and the rod as the spring. Thermal noise acts as a stochastic force that excites this damped harmonic oscillator.

The longitudinal acoustic mode of vibration of the oscillator is excited by thermal noise, as shown in figure 1.8. In section 1.1 we described the equation of motion of the oscillator and the longitudinal vibration due to thermal noise in thermodynamic equilibrium.

The rod is kept in vertical position with the cuboid mass at the bottom, free to oscillate. The top part of the rod is bolted to an aluminum disk supported by a mechanical suspension. At the very top, coaxial with the rod, a piezoelectric actuator is mounted (visible in figure 2.3.b): it can provide vertical mechanical excitations to the system, i.e. to the oscillator, and so it can be used to study response of the oscillator and to test the measuring apparatus.

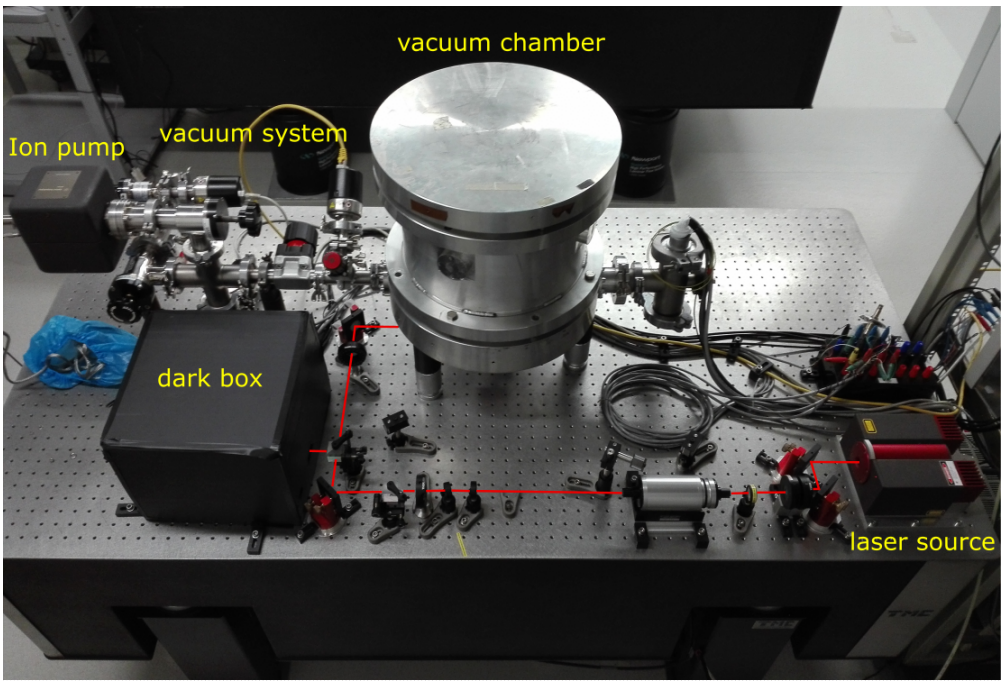

Figure 2.1: The overall apparatus. In the center on the optical table, there is the vacuum chamber which on its left is connected with the vacuum system ending with the ion pump. The laser path starts from the laser source on the right, reaches the oscillator inside the vacuum chamber, from below, and then it is directed to the photodiodes on the table and in air, under the dark box shown on the left.

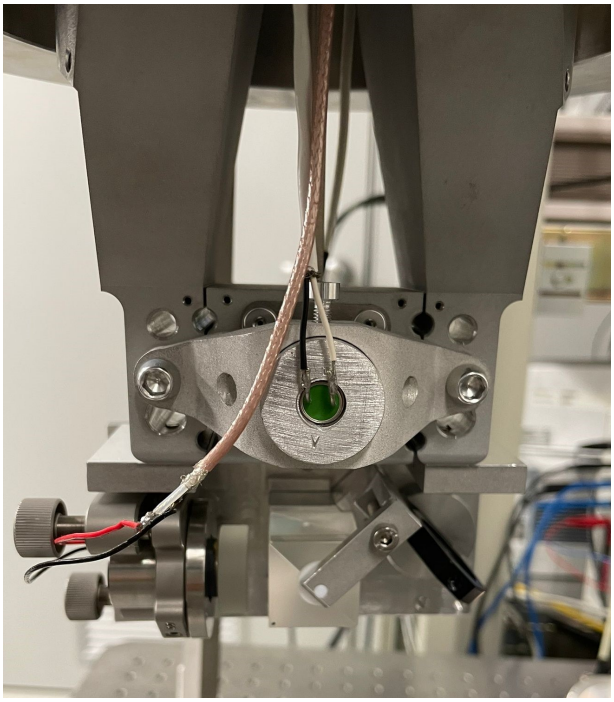

Figure 2.2: Photo of the oscillator and of the optical elements below. The cuboid load mass in the centre of the photo is suspended by the vertical rod (in photo they are partially hidden by the mechanical suspensions and by the electrical wires); two vertical protrusions suspend the heater (the green and grey cylindrical object in front of the cubic mass) and the Michelson interferometer below; the latter is made up (from left to right) by a reference mirror suspended by a piezoelectric actuator, a beam splitter and an absorber.

2.2 Heater

In order to set non-equilibrium states across the oscillator, we face an infrared heater to one side of the cuboid mass (as shown in figure 2.2). It consists of a 3.6 Ω resistance heated by a current via Joule

effect (for example, 1.8A at 6V with a temperature of 975°C) of which the consequent emitted radiation is directed toward the cubic mass of the oscillator by a parabolic mirror surrounding the resistance. We use two thermometers to measure the temperature T_1 of the rod top (with a NTC thermistor) and the temperature T_2 of the cuboid mass (with a thermopile). The use of radiative heating, as well of the thermopile, allow to not provide additional vibrations and losses to the oscillator.

2.3 Mechanical suspension

A mechanical filter is a mechanical oscillator with a resonance frequency much lower than the frequencies of interest. For frequencies ν much higher than the resonance frequency of the filter ν_0 and in the low-loss regime, that is with $\nu_0 \ll \nu \ll \frac{\nu_0}{\phi}$ (with ϕ the filter loss angle), an input vibration of the oscillator is depressed in output by the factor

$$T(\nu_0, \nu) = \frac{\nu_0^2}{\nu_0^2 - \nu^2}, \tag{2.1}$$

called the transfer function of the oscillator. From a high enough frequency, the filter oscillator stops to behave as a rigid body and it shows internal resonance frequencies, that increase the transfer function.

In order to reduce the noise coming from the ground, of which the main source is the seismic activity, the oscillator is suspended by a cascade of three passive mechanical filters [16]. Since seismic noise is isotropic and in a mechanical structure the degrees of freedom are easily coupled, the filters has to be effective in all the three spatial directions and the three rotation angles. Each of them is made up by a ring-shaped mass suspended by three C-shaped springs. The three filters are placed one over the other and the oscillator leans under the top filter and is hung coaxially with the annular masses as shown in figure 2.3.

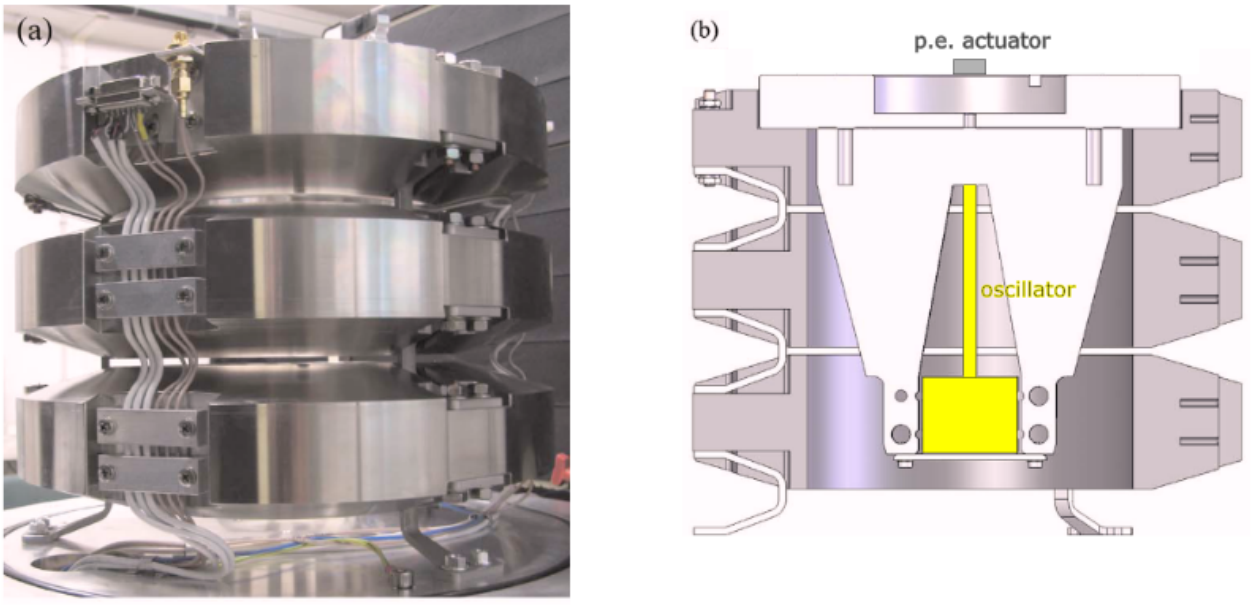

Figure 2.3: In (a) there is a photo of the three mechanical filters one over the other. Each filter is made up by a ring-shaped mass that leans on three C-shaped springs. In (b) there is a section of the three filters with inside the oscillator (yellow), connected to a structure leaned on the top filter and over which a piezoelectric actuator is placed.

The filters are designed to work in our frequency band of interest 300-2000 Hz. In particular, the values of the three masses and of an additional load placed over the filters are high in order to increase the values of the internal resonance frequencies, but not too high to not stress the spring material more than the 30% of the yield strength, to avoid non linear effects. The resonance frequency of a single stage is $\nu_0 = 38$ Hz; anyway, the overall cascade of filters shows a more complicated behavior, as shown in figure 2.4, where the measured transfer function is plotted.

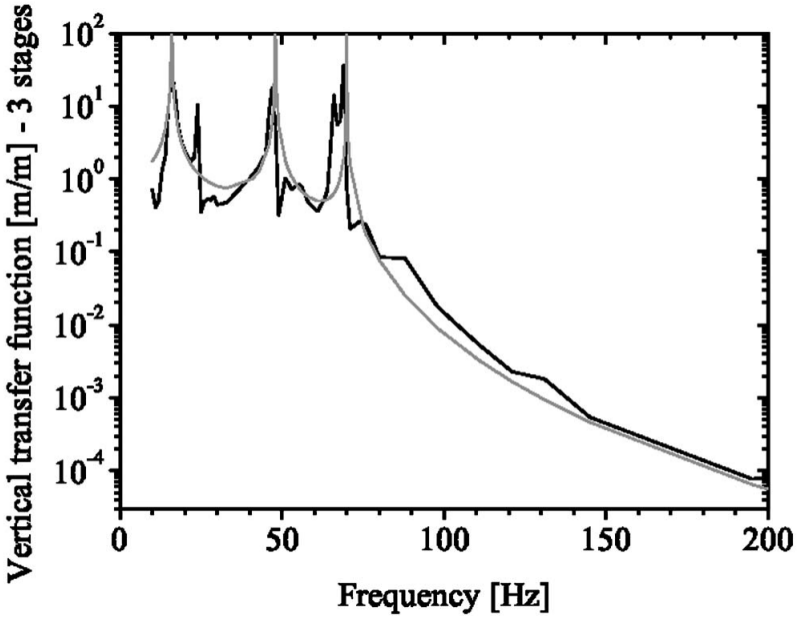

Figure 2.4: Transfer function of the cascade of the three mechanical filters suspending the oscillator. The black line is the measured function while the grey one is the theoretical prediction. [16]

The vacuum chamber (section 2.4) in which the oscillator and the three filters are placed leans on three pillars in which a cube of Sylodamp (SP 1000) acts as mechanical filter (see figure 2.5). The same cubes of Sylodamp are used in the pillars that sustain the vacuum system. This allows to further reduce the vibrations, in particular those related to the three peaks in the range $10 \div 70$ Hz in figure 2.4 and their higher harmonics, peaks that the cascade of three mechanical filters is not able to avoid.

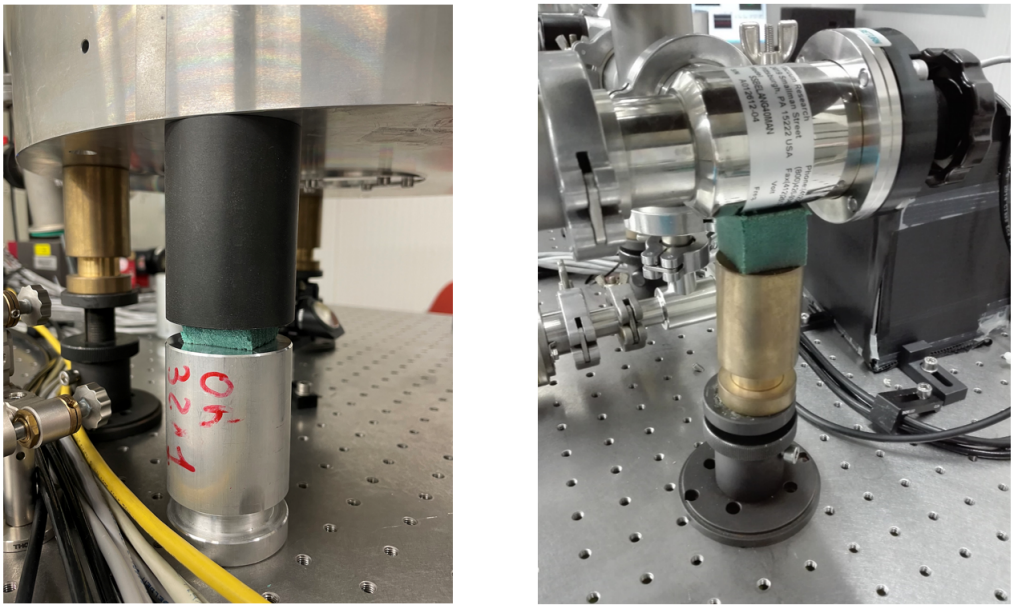

Figure 2.5: LEFT: one of the three pillars sustaining the vacuum chamber; between the grey and the black cylindrical parts the aqua green cube of Sylodamp is placed. RIGHT: one of the pillars sustaining the vacuum system, with the cube of Sylodamp at its top just under the vacuum pipe.

Moreover, the vacuum chamber, the vacuum system and the optical system are placed over an optical table, of which the platform is air suspended by the legs which act as active filters.

2.4 Vacuum system

A source of mechanical noise is the sound waves propagating in air, causing the acoustic noise. To reduce it, the oscillator and the three mechanical filters that sustain it are contained in a vacuum chamber connected to an ion pump, that is vibration free and so it does not transmit vibration to the oscillator. To switch on the ion pump, we use a turbomolecular pump connected to a rotary pump. The scheme of the vacuum system is shown in figure 2.6. Three Penning gauges allow to measure the pressures and three valves are used to manage the vacuum system. The pressure in the chamber reaches the order of $10^{-}6$ mbar.

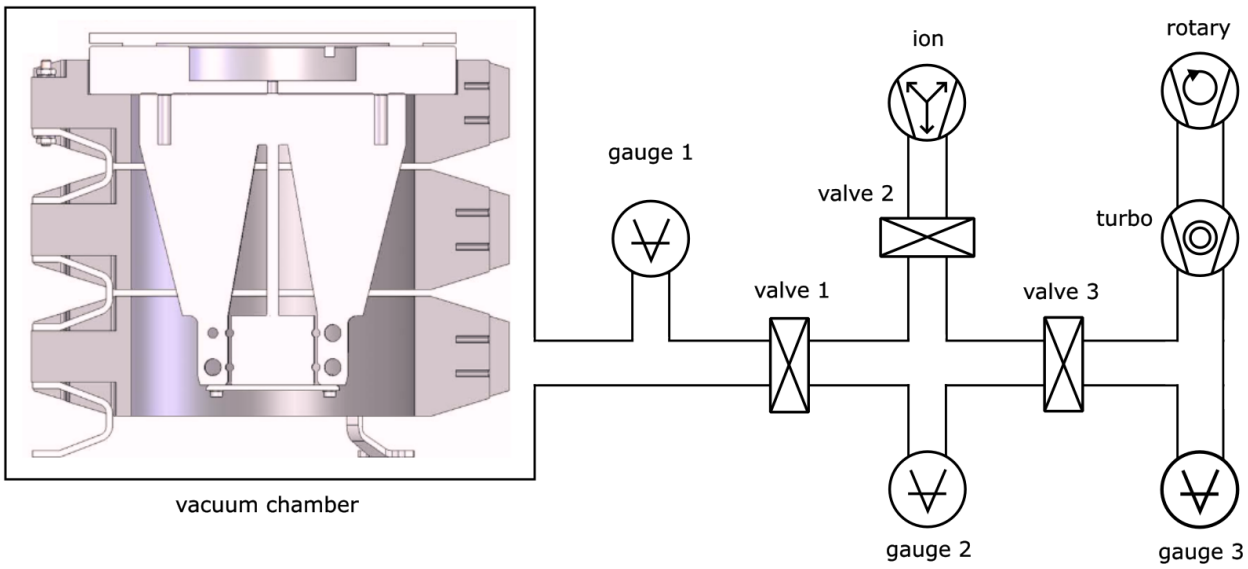

Figure 2.6: Vacuum system scheme. The three pressure gauges and the three valves allow to monitor and control the system. The turbomolecular and the rotary pumps needs to reach the necessary pressure in the chamber of 10^{-4}mbar in order to switch on the ion pump (VacIon Plus 20 Diode), then the valve 3 is closed and the ion pump is the only switched on pump, avoiding the vibrations coming from the turbomolecular pump.

2.5 Outputs and acquisition system

The acquisition system is based on a National Instruments PXI platform. The polarization-multiplexed interferometer provides voltage outputs from four photodiodes that are acquired using a 24-bit resolution ADC NI PXI-4462 DAQ board; the rate of acquisition is 8000 Samples/sec in the range of $\pm 10V$ (fast channels).

The pressures in the vacuum system are monitored via three Penning gauges (as shown in figure 2.6). For the measurement of temperature, a sensor is placed outside the vacuum chamber in the room, while in the vacuum chamber there are three sensors: for the air, the fixed end of the rod and the cubic mass. The latter sensor is a thermopile while the other three are NTC thermistors. All the pressures and the temperatures are acquired at 1 Samples/sec by NI 9219 24-bit universal analog inputs (slow channels).

NI LabView was used to develop the acquisition software and to show the fast and slow data during the acquisition. The data are stored in BIN file and the analysis is carried out with Python.

2.6 Upgrades

In the Michelson interferometer just below the oscillator, an absorber was placed in front of the free port of the beam splitter to reduce the stray light (see figure 2.2). Furthermore, the reference mirror of the Michelson interferometer was mounted on a piezoelectric actuator. This can be used to

provide displacements to the reference mirror that can be used for the calibration of the measuring apparatus (described in section 3.2) and to test its calibration procedure and its response (as carried out in sections 4.3 and 4.4 respectively).

Chapter 3

The interferometric readout

In the previous chapter I have described the experimental apparatus, in which thermal noise induces vibrations in a harmonic oscillator, both in and out thermodynamic equilibrium. In this chapter I focus on the interferometric readout of the oscillator vibrations: as described in more details later on, the bottom surface of the oscillator (namely, of the cuboid mass) is made to be as a mirror in a quadrature phase interferometer. In particular, the surface of the oscillator constitutes one of the mirrors of the interferometer, so that a displacement of the surface causes a change of the measured interference. We cannot use as readout a simple Michelson interferometer because it is monotone only within one fringe. To overcome this limit we use a quadrature phase interferometric technique, that exploits two linear and orthogonal polarizations of the laser field, to measure separately the cosine and sine of the phase corresponding to the changed path length. By unwrapping, i.e. by using the sine and cosine information to compute the phase, we can hence follow the full phase of the interference beyond the interval between two consecutive extremes of a single interference output.

In section 3.1 we describe the optical system of the interferometer and we derive its output in an ideal case. In section 3.2 we consider the limits of the ideal case and we describe the calibration needed by the interferometer. Finally, in section 3.3 we describe the spectral analysis performed on the photodiode outputs of the interferometer, that leads to the estimation of thermal noise.

3.1 Interferometric readout - ideal case

The optical system of the interferometer is shown in figure 3.1. The laser source emits a linearly polarized beam and it passes through a quarter-wave plate ($\lambda/4$ #1) and a half-wave plate ($\lambda/2$ #1), which, jointly to the subsequent lens, introduces the beam in the Faraday Isolator. After two lenses which collimate the beam, the combination of a half-wave plate ($\lambda/2$ #2) with a polarizing beam splitter (PBS #1) works as a power controller. The beam passes through a 50% beam splitter (BS #1) and a half-wave plate ($\lambda/2$ #3), which rotate the polarization in the desired angle. The subsequent mirror reflects the beam vertically inside the vacuum chamber, in which a polarizing beam splitter (PBS #2) reflects the s polarization toward the reference mirror and transmits the p polarization toward the oscillator. Then the two beams come back to the PBS #2, where they are directed outside the vacuum chamber and overlapped. So the recombined beam goes back through $\lambda/2$ #3 and reaches BS #1, which reflects the beam inside the dark box. A lens collimates the beam which is splitted by the BS #2; half of the power is splitted by PBS #3, which reflects the s polarization and transmits the p one, of which the powers are measured by the photodiodes A and B; the other half of the power passes through a quarter-wave plate ($\lambda/4$ #2) and only then is splitted by PBS #4 according to the p and s polarizations of which the powers are measured by the photodiodes C and D.

Now we provide an analysis of the interferometric readout considering ideal optical elements, i.e. with nominal reflectivity and transmissivity and without losses, and with a perfect overlap of the two interfering beams. The deviations from this ideal situation proper to the real one will be discussed in the following section.

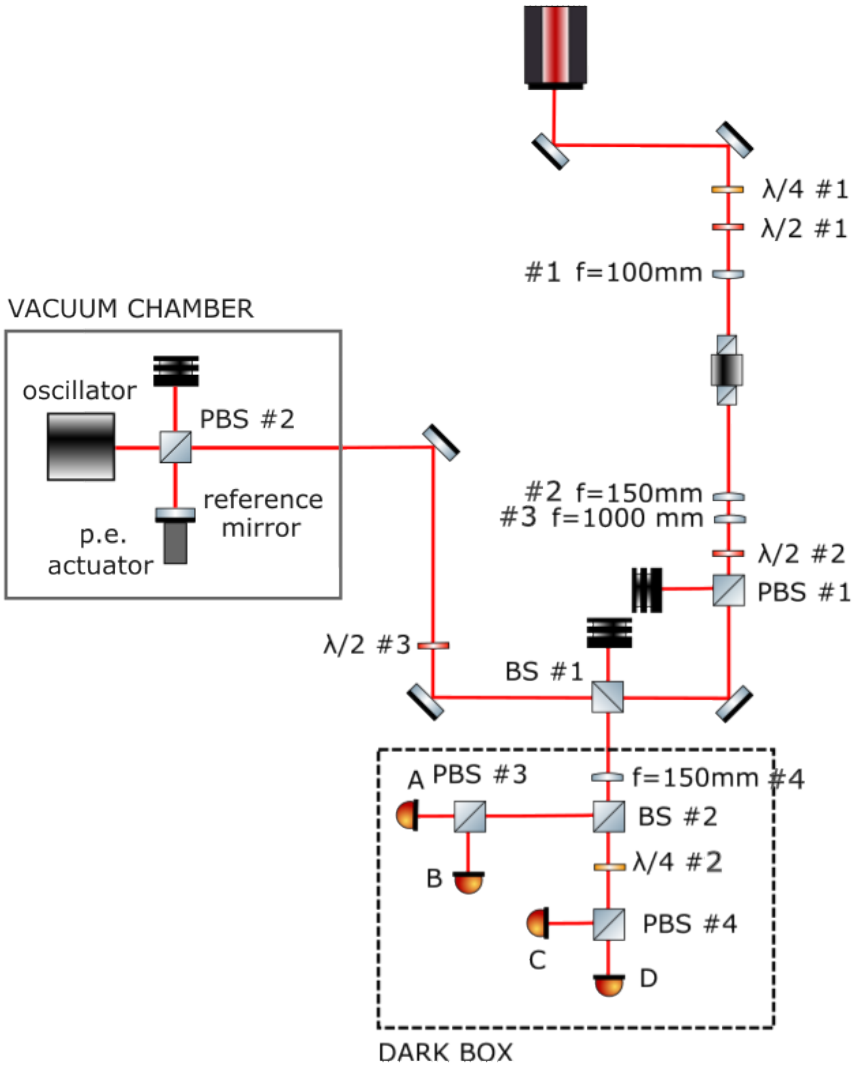

Figure 3.1: Scheme of the quadrature phase differential interferometer. From the laser source the beam reaches the vacuum chamber with a linear polarization at 45° respect the vertical direction. Here the laser beam is splitted and half of its power is reflected by the oscillator. Then the laser comes back and goes into the dark box in which it is acquired by the photodiodes.

The laser source (see figure 3.1) provides a linearly polarized Gaussian beam with $\lambda = 1064$ nm and power 201 mW. The combination of quarter-wave plate #1 and half-wave plate #1 allows to minimize the ellipticity of the polarizazion of the beam emerging from the laser source and rotates the orientation of the linear polarization to match that of the Faraday Isolator. The latter avoids that light comes back from the optical system and goes into the laser source.

The lenses are placed to collimate the beam. The lens #3 is added beside the lens #2 to change the position of the waist of the beam, from the PBS #2 before the beam has reached the oscillator to the entrance of the chamber when the beam is exiting from it, that is more distant from the oscillator; this is performed to reduce the stray light, i.e. scattered light recoupled to the main beam.

The combination of half-wave plate #2 with PBS #1 allows to have in transmission a p-polarized beam with adjustable power. The PBS reflects the *s* polarization (along the y axis) into an absorber and transmits the *p* polarization (x axis). So, the transmitted intensity is proportional to the cosine square of the angle between the polarization entering the PBS and the horizontal direction, and varying this angle rotating the half-wave plate you control the intensity of the beam proceeding in the optical system.

This allows to have enough power that reaches the photodiodes to use the full dynamic range of

the ACQ boards, without saturating the photodiodes. After PBS #1 the electric field of the beam in the complex notation for the two polarizations along the x (horizontal) and y (vertical) axes is

$$E_{in} = \mathbb{J}_{PBS_t} E_0 = E_0 \begin{pmatrix} 1 \\ 0 \end{pmatrix}, \tag{3.1}$$

where $\mathbb{J}_{PBS_t}$ is the Jones matrix of the PBS indicated in table 3.1, $E_0 = E_0\left(\rho = \sqrt{x^2+y^2}, z, t\right)$ describes the distribution of the Gaussian beam in the transverse plane (x, y) and its evolution in time and in the longitudinal direction z.

Optical component	Jones matrix
half-wave plate	$\mathbb{J}_{\lambda/2}(22.5°) = \frac{1}{\sqrt{2}} \begin{pmatrix} 1 & 1 \\ 1 & -1 \end{pmatrix}$ $\mathbb{J}_{\lambda/2}(-22.5°) = \frac{1}{\sqrt{2}} \begin{pmatrix} 1 & -1 \\ -1 & -1 \end{pmatrix}$
quarter-wave plate	$\mathbb{J}_{\lambda/4}(45°) = \frac{1}{2} \begin{pmatrix} 1+i & 1-i \\ 1-i & 1+i \end{pmatrix}$
polarizing beam splitter	$\mathbb{J}_{PBS_t} = \begin{pmatrix} 1 & 0 \\ 0 & 0 \end{pmatrix}$ $\mathbb{J}_{PBS_r} = \begin{pmatrix} 0 & 0 \\ 0 & 1 \end{pmatrix}$
beam splitter	$\mathbb{J}_{BS_t} = \frac{1}{\sqrt{2}} \begin{pmatrix} 1 & 0 \\ 0 & 1 \end{pmatrix}$
mirror	$\mathbb{J}_M = \begin{pmatrix} 1 & 0 \\ 0 & -1 \end{pmatrix}$

Table 3.1: List of the optical components with their Jones matrices in the ideal behavior. PBS_t refers to the transmitted beam by the PBS, which has only the p polarization (x component), while PBS_r refers to the reflected beam, which has only the s polarization (y component).

Then the beam is splitted by the 50% beam splitter #1 which reflects half of the intensity, which is absorbed by an absorber, and transmits the other half; then the latter passes through the $\lambda/2$ #3, which has the effect of rotating the polarization at the angle of 45° with the x axis. The beam entering in the vacuum chamber results

$$E_{chamber,in} = \mathbb{J}_{\lambda/2}(22.5°)\mathbb{J}_{BS} E_{in} = \frac{E_0}{2} \begin{pmatrix} 1 \\ 1 \end{pmatrix}, \tag{3.2}$$

where $\mathbb{J}_{\lambda/2}(22.5°)$ and $\mathbb{J}_{BS}$ are the Jones matrices described in table 3.1, referred to half-wave plate #3 and BS #1 respectively.

In the vacuum chamber the p polarization is transmitted by the PBS #2, it is reflected by the lower surface of the oscillator and then it is transmitted by the PBS; the s polarization is reflected by the PBS, it is reflected by the reference mirror mounted on the piezoelectric actuator and then is reflected by the PBS out of the chamber overlapping to the p polarization. (These elements are shown in figure 2.2.) The beam that exits the vacuum chamber is

$$\begin{aligned} E_{chamber,out} &= \mathbb{J}_{PBS_t}\mathbb{J}_M e^{-ik2L_O}\mathbb{J}_{PBS_t} E_{chamber,in} + \mathbb{J}_{PBS_r}\mathbb{J}_M e^{-ik2L_M}\mathbb{J}_{PBS_r} E_{chamber,in} = \\ &= \frac{E_0}{2} \begin{pmatrix} e^{-ik2L_O} \\ -e^{-ik2L_M} \end{pmatrix} = \frac{E_0 e^{-ik2L_O}}{2} \begin{pmatrix} 1 \\ -e^{ik2(L_O - L_M)} \end{pmatrix} \equiv \frac{E_0}{2} \begin{pmatrix} 1 \\ -e^{i\psi} \end{pmatrix}, \end{aligned} \tag{3.3}$$

where $\mathbb{J}_{PBS_t}$ and $\mathbb{J}_{PBS_r}$ are the Jones matrices of the PBS #2 respectively in transmission and reflection (see table 3.1), $\mathbb{J}_M$ is the Jones matrix of the reference mirror or of the mirror constituted by the surface of the oscillator, $k = \frac{2\pi}{\lambda}$ is the wave number, L_O and L_M are the distances from the PBS #2 to the oscillator and the reference mirror respectively, $\psi = k2(L_O - L_M)$ and in the last passage $E_0 e^{-ik2L_O}$ has been called E_0.

The beam now has an elliptical polarization, with the axes oriented at 45° respect to the horizontal direction. The beam goes back passing through the $\lambda/2$ waveplate #2 which now is seen with an angle opposite to that seen the first time from the other direction, and thus the waveplate rotates the elliptical polarization so that one of its axes is in the horizontal direction (x axis)[1]. The resulting field is

$$E_{chamber,out2} = \mathbb{J}_{\lambda/2}(-22.5°)E_{chamber,out} = \frac{E_0}{2\sqrt{2}} \begin{pmatrix} e^{i\psi}+1 \\ e^{i\psi}-1 \end{pmatrix}, \tag{3.7}$$

where $\mathbb{J}_{\lambda/2}(-22.5°)$ is the Jones matrix of the half-wave plate #3 seen in the back direction (shown in table 3.1).

Then the beam reaches the BS #1, where half of the power is transmitted (a part of which reaches the Faraday Isolator which avoids that it goes into the laser source) and half is reflected into the dark box. Here the lens #4 collimates the beam in order to have the beam size small enough to enter the photodiodes. The BS #2 reflects half of the power toward the PBS #3, which reflects the s polarization and transmits the p one, of which the power is measured respectively by the photodiodes B and A. In this way, the photodiode A measures the power associated to the x component of the polarization, proportional to the horizontal axis of the polarization ellipse, while the photodiode B measures the power associated to the y component of the polarization, proportional to the vertical axis of the polarization ellipse. So, since the magnitudes of the two axes depend on the phase ψ of the interferometer, we are able to infer ψ from the outputs of the photodiodes. In formulas, the detected fields result

$$E_A = \mathbb{J}_{PBS_t}\mathbb{J}_{BS}\mathbb{J}_{BS}E_{chamber,out2} = \frac{E_0}{4\sqrt{2}} \begin{pmatrix} e^{i\psi}+1 \\ 0 \end{pmatrix}, \tag{3.8}$$

$$E_B = \mathbb{J}_{PBS_r}\mathbb{J}_{BS}\mathbb{J}_{BS}E_{chamber,out2} = \frac{E_0}{4\sqrt{2}} \begin{pmatrix} 0 \\ e^{i\psi}-1 \end{pmatrix}. \tag{3.9}$$

The corresponding powers P measured by the photodiodes are given by the integral of the intensity I over the area of the photodiode A_{PD},

$$P = \int_{A_{PD}} I dA = \int_{A_{PD}} \frac{c\epsilon}{2}|E|^2 dA, \tag{3.10}$$

with c the velocity of light in the air and ϵ the dielectric constant; so for the photodiodes A and B you have:

$$P_A = \int_{A_{PD}} \frac{c_0\epsilon_0}{2}\frac{E_0^2}{16}(1+\cos\psi)dA \equiv \frac{P_0}{16}(1+\cos\psi), \tag{3.11}$$

$$P_B = \frac{P_0}{16}(1-\cos\psi), \tag{3.12}$$

[1]This can be shown calculating the phase difference between the y and x polarizations P_y and P_x from eq. 3.7:

$$\begin{aligned} &\angle P_y - \angle P_x = \angle\left(e^{i\psi}-1\right) - \angle\left(e^{i\psi}+1\right) = \operatorname{atan2}(\sin\psi, \cos\psi - 1) - \operatorname{atan2}(\sin\psi, \cos\psi + 1) = \\ &= \pi - \arctan\frac{\sin\psi}{1-\cos\psi} - \arctan\frac{\sin\psi}{1+\cos\psi} = \pi - \arctan\pm\sqrt{\frac{1+\cos\psi}{1-\cos\psi}} - \arctan\pm\sqrt{\frac{1-\cos\psi}{1+\cos\psi}} \equiv \\ &\equiv \pi \mp \left(\arctan a + \arctan\frac{1}{a}\right) \equiv \pi(a), \end{aligned} \tag{3.4}$$

where atan2 is the four quadrant arctangent and in the last expression there is the minus sign if $\sin\psi \geq 0$ and the plus sign if $\sin\psi < 0$. The cotangent of $f(a)$ results:

$$\operatorname{cotan} f(a) = \frac{\operatorname{cotan}(a)\operatorname{cotan}\left(\frac{1}{a}\right) - 1}{\operatorname{cotan}(a) + \operatorname{cotan}\left(\frac{1}{a}\right)} = \frac{\frac{1}{\tan(a)}\frac{1}{\tan\left(\frac{1}{a}\right)} - 1}{\frac{1}{\operatorname{cotan}(a)} + \frac{1}{\operatorname{cotan}\left(\frac{1}{a}\right)}} = \frac{\frac{1}{a}a - 1}{\frac{1}{a} + a} = 0. \tag{3.5}$$

So you get

$$\angle P_y - \angle P_x = \pi \mp \frac{\pi}{2}, \tag{3.6}$$

which is the condition in which the axes of the polarization ellipse are along the x and y direction.

where $P_0 = \int_{A_{PD}} \frac{c_0 \epsilon_0}{2} E_0^2 (1 + \cos\psi) dA$ is the power of the beam transmitted by the PBS #1.

From these formulas of the measured quantities P_A and P_B you can find the cosine of ψ, but you are not able to find the phase ψ unambiguously because of the periodicity of the cosine function. This is the reason to implement the quadrature phase interferometry, with which we measure both the sine and cosine of ψ. This allows to overcome the ambiguity in the reconstruction of ψ, in fact, when you reach an extreme of the cosine of ψ (or the sine), with the related uncertainty to determine ψ, you can consider the sine (or the cosine) to keep following the evolution of ψ.

This is realized considering the beam that is transmitted by the BS #2. It passes through the quarter-wave plate #2, which is oriented with its slow and fast axes at 45° with respect to the horizontal direction, i.e. with respect to the axes of the polarization ellipse of the beam. This causes a change of the polarization, which remains still elliptical and still with the axes along the x and y directions, but with a dependence of their magnitude on the phase ψ that is different compared with before. After the quarter-wave plate, analogously to the case of the photodiodes A and B, the beam is splitted by the PBS #4 so that the power associated to the x component of the polarization, proportional to the horizontal axis of the polarization ellipse, is measured by the photodiode D, while the power associated to the y component of the polarization, proportional to the vertical axis of the polarization ellipse, is measured by the photodiode C. The detected fields result

$$E_C = \mathbb{J}_{PBS_r} \mathbb{J}_{BS} \mathbb{J}_{BS} E_{chamber,out2} = \frac{E_0}{4\sqrt{2}} \begin{pmatrix} 0 \\ e^{i\psi} - i \end{pmatrix}, \tag{3.13}$$

$$E_D = \mathbb{J}_{PBS_t} \mathbb{J}_{BS} \mathbb{J}_{BS} E_{chamber,out2} = \frac{E_0}{4\sqrt{2}} \begin{pmatrix} e^{i\psi} + i \\ 0 \end{pmatrix}. \tag{3.14}$$

The corresponding measured powers are

$$P_C = \frac{P_0}{16}(1 - \sin\psi), \tag{3.15}$$

$$P_D = \frac{P_0}{16}(1 + \sin\psi). \tag{3.16}$$

These new two quantities P_C and P_D depend on the phase ψ, not through its cosine as in formulas (3.11) and (3.12), but through its sine, which thus can be inferred. Inverting the relations (3.11), (3.12), (3.15) and (3.16), the cosine and the sine of ψ are given by

$$\cos\psi = \frac{P_A - P_B}{P_A + P_B} \equiv C_x \tag{3.17}$$

$$\sin\psi = \frac{P_D - P_C}{P_D + P_C} \equiv C_y, \tag{3.18}$$

where C_x is the interfererometer contrast for the photodiodes A and B, while C_y for the the photodiodes C and D. In the formulas (3.17) and (3.18) the term P_0 contained in the powers measured by the photodiodes simplifies and so the contrasts result independent on the power of the laser and its fluctuations. In figure 3.2 left the powers of the four photodiodes are plotted as functions of the phase ψ, while in figure 3.2 right there are the values that the contrasts can assume, which are in dependence of ψ. In this ideal case, the single measured powers have a unitary visibility, i.e.

$$\mathcal{V} = \frac{P_{max} - P_{min}}{P_{max} + P_{min}} = 1, \tag{3.19}$$

and the contrasts describe a circle with unitary radius centred in (0, 0) in the contrasts plane.

From the relations (3.17) and (3.18) we now extract the phase ψ exploiting both the informations on the sine and on the cosine of ψ. This is performed via the four quadrant arctangent, which inverts the tangent of ψ taking into account the signs of the cosine and of the sine of the angle, not only their ratio, reaching a codomain of 2π. Furthermore, for every values of the angle the codomain is

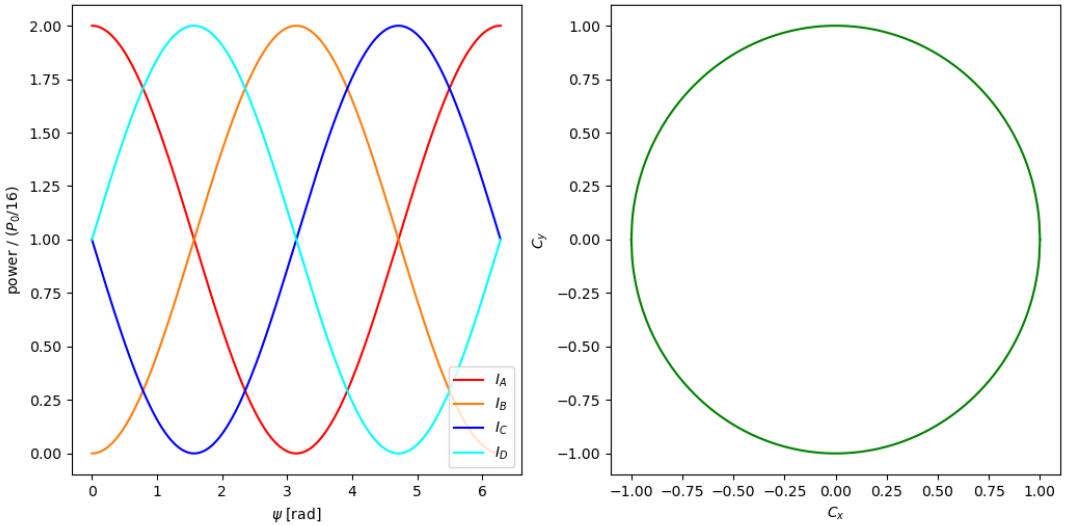

Figure 3.2: LEFT: The ideal light powers measured by the four photodiodes, given by the formulas (3.11), (3.12), (3.15) and (3.16). RIGHT: The ideal contrasts C_x and C_y which, in accordance with (3.17) and (3.18), are equal to the cosine and the sine of ψ and so in the contrasts plane they describe a circle with unitary radius and centred in (0, 0).

chosen in order to have a let's say continuous angle, without sharp jumps of 2π (dynamics compatible with our measurement, that follows the continuous displacement of a surface); this leads to have not a codomain of 2π but from -∞ to $+\infty$. This is carried out with the function numpy.unwrap() in python. You have:

$$\psi = \text{unwrap}(\text{atan2}(\sin\psi, \cos\psi)). \tag{3.20}$$

From the phase ψ you get the relative displacement between the reference mirror and the lower surface of the oscillator:

$$\Delta L = L_O - L_M = \frac{\psi}{2k} = \frac{\lambda}{4\pi}\text{unwrap}\left(\text{atan2}\left(\frac{P_D - P_C}{P_D + P_C}, \frac{P_A - P_B}{P_A + P_B}\right)\right). \tag{3.21}$$

The thermal noise we want to measure varies the values of L_O and thus also of ΔL of the same quantity.

3.2 Interferometric readout - real case and calibration

The ideal case in the previous section does not consider the losses in the optical elements and their true rather than nominal properties. Mirror reflectivity is not exactly unitary and it is different for the s and p polarization. Waveplate transmissivity is not unitary and it is different for the s and p polarization. Beam splitter reflectivity and transmissivity is not exactly the 50% and they are different for the s and p polarization. Analogously, polarization beam splitter transmissivity is not unitary for the p polarization and null for the s one, while its reflectivity is not null for the p polarization and unitary for the s one.

These properties, together with a not perfect alignment of the optical elements, make the formulas (3.11), (3.12), (3.15) and (3.16) not exactly valid, in particular the visibilities of the measured power result lower than the unitary value, and so the interferometer contrasts C_x and C_y do not respect properly the relations (3.17) and (3.18). So, with the changing of the phase ψ, the contrasts do not provide the perfect circle of unitary radius shown in figure 3.2 right, but approximately an ellipse with the semiaxes lower than the unitary value and with the centre not perfectly in the origin of the axes $(C_x, C_y) = (0, 0)$. An example is shown in figure 3.3; these data are taken by scanning L_M by feeding

the piezoelectric actuator sustaining the reference mirror (described in section 2.6) with a sinuisodal signal, so that the phase ψ and consequently the four interferences measured by the photodiodes vary. The left figure shows the outputs of the four photodiodes for nearly a semi-period of the sinusoidal voltage, while the right figure shows the corresponding contrasts, which describe an elliptical curve. In the real case the contrasts can be linked to the phase ψ by the parametric equations of an ellipse:

$$C_x = X_0 + X\cos\psi, \tag{3.22}$$

$$C_y = Y_0 + Y\sin(\psi + \phi). \tag{3.23}$$

Inverting these two relations you obtain the cosine and the sine of the phase ψ for given contrasts:

$$\cos\psi = \frac{C_x - X_0}{X} \tag{3.24}$$

$$\sin\psi = \frac{1}{\cos\phi}\left(\frac{C_y - Y_0}{Y} - \frac{C_x - X_0}{X}\sin\phi\right). \tag{3.25}$$

So, to find $\cos\psi$ and $\sin\psi$ you need the parameters of the ellipse X_0, Y_0, X, Y and ϕ. Their estimation is carried out measuring C_x and C_y (using the formulas (3.17) and (3.18)) while you vary the arm lengths L_M or L_O by at least a full fringe. Then the data of C_x and C_y are fitted with the formulas (3.22) and (3.23), getting the parameters of the ellipse. In figure 3.3 right there is an example of this kind of data fitted by an ellipse. The movement of the mirror of the Michelson interferometer can be realized providing a voltage signal to the piezoelectric actuator sustaining the reference mirror or heating the oscillator with the thermopile so that it expands toward the PBS #2.

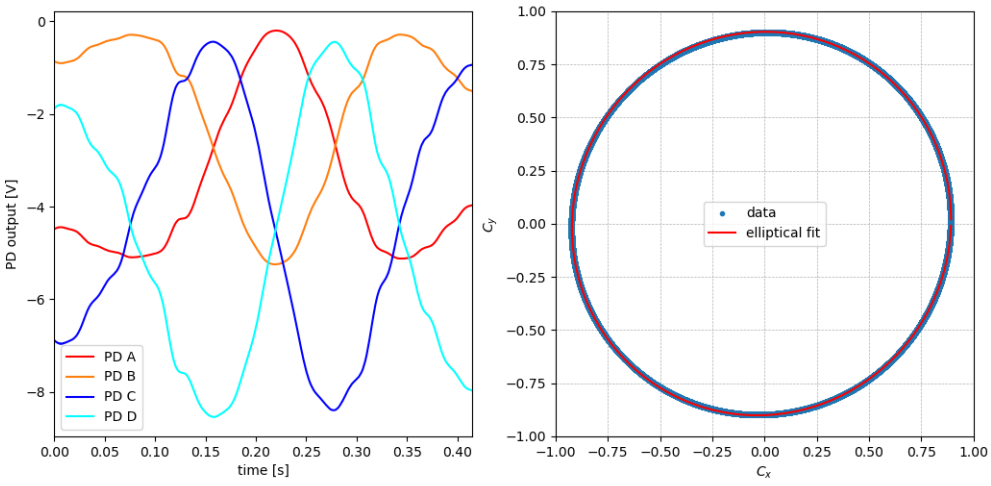

Figure 3.3: Example raw data and calibration. LEFT: outputs of the four photodiodes while a large sinusoidal voltage of 1Hz ($180V_{pp}$ and offset $90V_{pp}$) is applied to the actuator sustaining the reference mirror of the interferometer; the data are related to almost a semi-period of the applied voltage. RIGHT: the contrasts C_x and C_y obtained from the outputs of the photodiodes with the conditions of the left figure for 30 s of data. The contrasts are fitted by the ellipse of (3.22) and (3.23), obtaining the parameters $(X_0, Y_0) = (-0.0146 \pm 0.0010)$, $(X, Y) = (0.9074, 0.9024)$ and $\phi = 0.0219$rad.

The values of $\cos\psi$ and $\sin\psi$ obtained from (3.24) and (3.25), analogously to the ideal case, can be used in the formula (3.20) to get the phase ψ from which you obtain the relative displacement of the oscillator $\Delta L = L_O - L_M = \frac{\lambda}{4\pi}\psi$.

Another correction is performed to compensate the output signal provided by the photodiodes. Considering for example the laser beam that goes through the PBS #3, it is divided so that (in first approximation) the p polarization goes into the photodiode A while the s polarization into the photodiode B. Because the PBS is not ideal, each of the outgoing beams has a power P_i (i= A, B)

which is reduced by losses, so that it can be expressed by the losses-free power $P_i^{(no\ losses)}$ multiplied by a factor l_i, with $0 < l_i \leq 1$:

$$P_A = l_A P_A^{(no\ losses)}, \tag{3.26}$$

$$P_B = l_B P_B^{(no\ losses)}. \tag{3.27}$$

So, the contrast C_x, according to the formula (3.17), results

$$C_x = \frac{P_A - P_B}{P_A + P_B} = \frac{l_A P_A^{(no\ losses)} - l_B P_B^{(no\ losses)}}{l_A P_A^{(no\ losses)} + l_B P_B^{(no\ losses)}} \neq \frac{P_A^{(no\ losses)} - P_B^{(no\ losses)}}{P_A^{(no\ losses)} + P_B^{(no\ losses)}} \equiv C_x^{(no\ losses)}. \tag{3.28}$$

This means that, since in general $l_A \neq l_B$ and so they don't simplify in formula (3.28), the value of the contrast C_x receives unwanted contribution from the losses of the PBS #3. The same dynamics characterizes the PBS #4 and the corresponding contrast C_y.

The power that reaches the PBS #3 is divided into the two photodiodes A and B, so that, in the ideal case, the sum of the powers measured by the two photodiodes, P_A and P_B, is expected to be constant. Because of the losses, present in the real case, the correct relation concerns the losses-free powers:

$$P_A^{(no\ losses)} + P_B^{(no\ losses)} = C, \tag{3.29}$$

where C is constant. Inserting in (3.29) the relations (3.26) and (3.27), you obtain

$$\frac{P_A}{l_A} + \frac{P_B}{l_B} = C, \tag{3.30}$$

from which:

$$P_B = l_B C - \frac{L_B}{L_A} P_A. \tag{3.31}$$

So the data of P_B in function of P_A can be fitted by the linear function

$$P_B = a_{BA} - b_{BA} P_A. \tag{3.32}$$

From this kind of fits, the parameter b_{BA} results slightly different from 1, attesting the non-ideal behavior of the PBS #3 (in figure 3.4 left there are example data, for which the slope is $b_{BA} = 1.00979 \pm 0.00006$). Now, the power measured by the photodiode A is corrected by:

$$P'_A = b_{BA} P_A, \tag{3.33}$$

In this way, considering that b_{BA} constitutes an estimate for $\frac{L_B}{L_A}$ (comparing (3.32) with (3.31)), the sum of the powers measured by the photodiodes A and B, results compatible with a constant value:

$$P'_A + P_B = \frac{l_B}{l_A} P_A + P_B = l_B \left(\frac{P_A}{l_A} + \frac{P_B}{l_B} \right) = l_B C, \tag{3.34}$$

where in the last passage we exploit the relation (3.30). Moreover, the contrast C_x, after the correction of (3.33), results equal to the losses-free one:

$$\begin{aligned} C'_x \equiv \frac{P'_A - P_B}{P'_A + P_B} &= \frac{\frac{l_B}{l_A} P_A^{(no\ losses)} - l_B P_B^{(no\ losses)}}{\frac{l_B}{l_A} l_A P_A^{(no\ losses)} + l_B P_B^{(no\ losses)}} = \frac{l_B P_A^{(no\ losses)} - l_B P_B^{(no\ losses)}}{l_B P_A^{(no\ losses)} + l_B P_B^{(no\ losses)}} = \\ &= \frac{P_A^{(no\ losses)} - P_B^{(no\ losses)}}{P_A^{(no\ losses)} + P_B^{(no\ losses)}} \equiv C_x^{(no\ losses)}, \end{aligned} \tag{3.35}$$

where in the second passage we exploit the relations (3.26) and (3.27).

Analogous considerations can be carried out considering the PBS #4 related to the contrast C_y, which lead to the compensation of the photodiodes C and D through the substitution:

$$P'_C = b_{DC} P_C, \tag{3.36}$$

in analogy with (3.33). So, with these two substitutions of (3.33) and 3.36, the undesired role of the losses of the PBSs #3 and #4 is avoided for the estimation of the contrasts C_x and C_y, and so of the relative displacement ΔL.

For this compensation of the outputs of the photodiodes we use the same data taken for the estimation of the calibration ellipse (see figure 3.3), which cover all the possible values of such outputs.

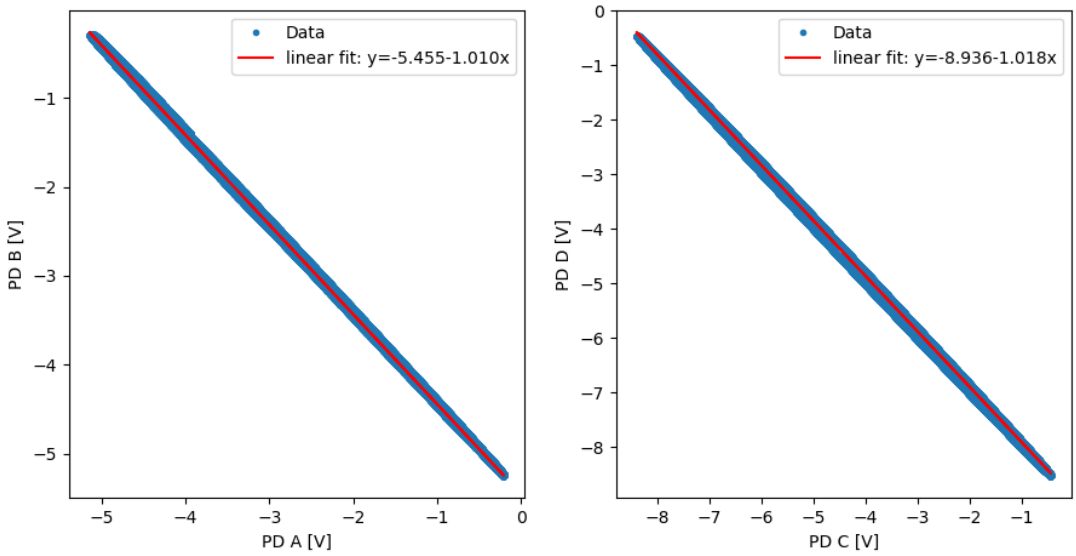

Figure 3.4: For the same example data plotted in figure 3.3, the output of the photodiode B is plotted in function of that of the photodiode A (LEFT), and the same for the photodiodes D and C (RIGHT). The data are fitted by a linear fit, of which the slope slightly differs from 1, with $b_{BA} = 1.00979 \pm 0.00006$ and $b_{DC} = 1.01772 \pm 0.00006$.

3.3 Spectral analysis

In our experiment the minimum ΔL we can measure is limited by different noise sources impacting at different time scales (or frequencies). To individuate that due to the thermal noise of the oscillator, we compute the PSD of ΔL. The latter can be seen as the sum of the PSD of ΔL, that is the difference between the relative distances L_O and L_M of the oscillator and the reference mirror from the PBS #2, and of a contribution S_{NN} taking into account the noises of the measuring apparatus, coming mainly from the photodiode shot noises, the ADC resolution and the residual mechanical noise. So you have

$$S_{\Delta L,\Delta L}(\nu) = S^{(ideal)}_{\Delta L,\Delta L}(\nu) + S_{NN}(\nu). \tag{3.37}$$

As said, we want to measure the thermal noise of the first longitudinal mode of the oscillator: its vibrations vary the distance L_O, with a PSD given by (1.12) or (1.13), which contributes to the measured PSD $S_{\Delta L,\Delta L}$ as shown in (3.37).

The estimation of $S_{\Delta L,\Delta L}(\nu)$ is carried out measuring data with the sampling frequency of 8000 samples/s and considering intervals of 10 s in the acquired data one after the other, with each interval with the first half overlapped with the previous interval and the second half overlapped with the following interval. For each 10 s interval the PSD is calculated and the data that show a high noise floor, i.e. not low enough to be sensible to thermal noise, are discarded. Then, for every sets of (for example) 20 consecutive accepted intervals a final estimate is provided by the average of their PSDs. This procedure allows to reduce the fluctuation in the estimated PSD. The latter results with the frequency resolution given by the inverse of the considered temporal interval, that is $R_{PSD} = 1/10\text{s} = 0.1\text{Hz}$. In figure 3.5 an example PSD is plotted.

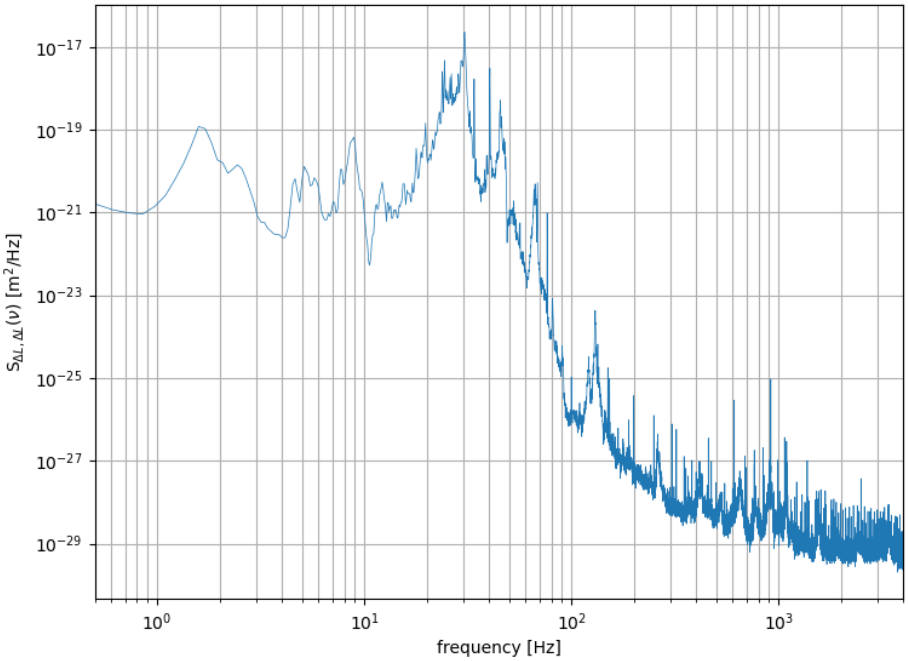

Figure 3.5: Example PSD of the measured relative displacement ΔL, considering 20 consecutive 10 s intervals.

The structure of the PSD (such as that of figure 3.5), with higher values at low frequencies, with peaks for example at 30 Hz and 45 Hz, and the reduction toward higher frequencies, is related to the cascade of three mechanical filters that sustain the oscillator, the transfer function of which shows a similar behavior (see figure 2.4). At the middle frequencies of $100 \div 300$ Hz the contribution of the stray lights is visible. At higher frequencies, the PSD is nearly flat. Such noise floor is due to the photodiode shot noise and to the white noise associated to the resolution of the acquisition system (i.e. a 24-bit one for the range $\pm$10V); it reaches the values of $10^{-30} \div 10^{-29}$ m^2/Hz. The estimation of thermal noise can be carried out if the noise floor at the frequency of interest (that is the resonance frequency of the oscillator) is low enough that the contribution of thermal noise to the PSD is visible over the noise floor, and the more it is higher than the noise floor the more the measure is accurate. Such contribution is due to a vibration of the surface of the oscillator that in thermodynamic equilibrium is expected (see equation (1.14)) with a displacement x for which $< x^2 >= 2.1 \cdot 10^{-28}$ m^2. As shown in section 4.2, this contribution has a FWHM of about 1 Hz and it reaches a height of about $2 \cdot 10^{-28}$, so that it is higher than the noise floor.

Chapter 4

Measurements

4.1 Transfer function of the oscillator

In order to estimate the thermal noise for the longitudinal mode of vibration of the oscillator we analyse the corresponding contribution in the PSD of the relative displacement ΔL, described in section 3.3. For this, we need to know the longitudinal resonance frequency of the oscillator (as justified in section 1.1, in particular by the formula (1.12) or (1.13)). So, we measure the longitudinal transfer function of the oscillator. The oscillator is sustained at the top end (at vertical position x_{top} with respect to its equilibrium position) by the rigid structure sustained by the mechanical filters over which a piezoelectric actuator is placed (see figure 2.3.b), to which a AC potential can be applied to transmit vertical vibrations to the system, with the consequent oscillation of the lower surface of the cubic load mass of the oscillator (at position x with respect to its equilibrium position), which we measure with the quadrature phase differential interferometer. The equation of motion of x is determined by the Hooke's restoring force and by the frictional force, and considering the velocity damping model (see section 1.1) it is

$$m\ddot{x}(t) = -k(x(t) - x_{top}(t)) - f\dot{x}(t), \tag{4.1}$$

where m is the mass of the cubic load, k is the spring constant of the oscillator and f the coefficient of the velocity damping frictional force. The equation in frequency domain results

$$-m\omega^2 x(\omega) = -k(x(\omega) - x_{top}(\omega)) - if\omega x(\omega), \tag{4.2}$$

and so you obtain the transfer function:

$$x(\omega) = \frac{k}{m\omega^2 - k - if\omega} x_{top}(\omega) = \frac{\nu_0^2}{\nu^2 - \nu_0^2 - iw\nu} x_{top}(\nu), \tag{4.3}$$

where in the last passage we use $\omega = 2\pi\nu$, $k = m(2\pi\nu_0)^2$ and $f = 2\pi wm$, consistently with the notation previously used (see eq. (4.10)).

The AC potential applied to the actuator at x_{top} is sinusoidal, given by $V = A_V + A_V \cos(2\pi ft)$, so the quantity $x(t)$ is expected with the form $x(t) = C + A\cos(2\pi ft + \phi)$, with C the DC contribution, A the amplitude of oscillation and ϕ the phase of the response. For a given frequency f of the applied potential, we measure x for 1 minute and we estimate its amplitude A exploiting the lock-in amplifier method. The quantity $x(t)$ is multiplied by $\cos(2\pi ft)$ or $\sin(2\pi ft)$, obtaining:

$$X = (C + A\cos(2\pi ft + \phi))\cos(2\pi ft) = C\cos(2\pi ft) + \frac{A}{2}(\cos(4\pi ft + \phi) + \cos\phi), \tag{4.4}$$

$$Y = (C + A\cos(2\pi ft + \phi))\sin(2\pi ft) = C\sin(2\pi ft) + \frac{A}{2}(\cos(4\pi ft + \phi) - \sin\phi). \tag{4.5}$$

To extract the DC part of X and Y, a low-pass filter with the cutoff frequency of 1 Hz is applied, obtaining

$$X_{DC} = \frac{A}{2}\cos\phi, \tag{4.6}$$

$$Y_{DC} = -\frac{A}{2}\sin\phi. \tag{4.7}$$

Finally, the amplitude of oscillation of x is given by

$$A = 2\sqrt{X_{DC}^2 + Y_{DC}^2}. \tag{4.8}$$

Exploiting this formula, we measure $A(f)$ for the frequencies of the applied potential in the range $1355\text{Hz} \leq f \leq 1425\text{Hz}$ every 0.1 Hz, where we expect to find the resonance frequency thanks to past measurements. Considering the modulus of the transfer function (4.3) and adding a constant term c, the data are fitted by the function

$$A(f) = \frac{\nu_0^2}{\sqrt{(\nu^2 - \nu_0^2)^2 + w^2\nu^2}} A_{top} + c, \tag{4.9}$$

where A_{top} is the amplitude of oscillation of the top end of the oscillator (x_{top}), which is considered constant with the varying of f because the amplitude of the applied potential is a fixed one and the response of the actuator is constant in our frequency range. The results are shown in figure 4.1. The data show a clear peak, from which the resonance frequency can be estimated; it is $\nu_0 = (1385.3 \pm 0.1)\text{Hz}$. The high χ^2_{red} doesn't allow to rely on its small uncertainty provided by the fit; the residuals plot shows a bad accordance of the fit especially on the tails of the data, and the latter show a clear peak, sharply defined with respect to the sampling rate of the data, taken every 0.1 Hz; so the uncertainty of the frequency resolution is estimated with 0.1 Hz, as a conservative choice.

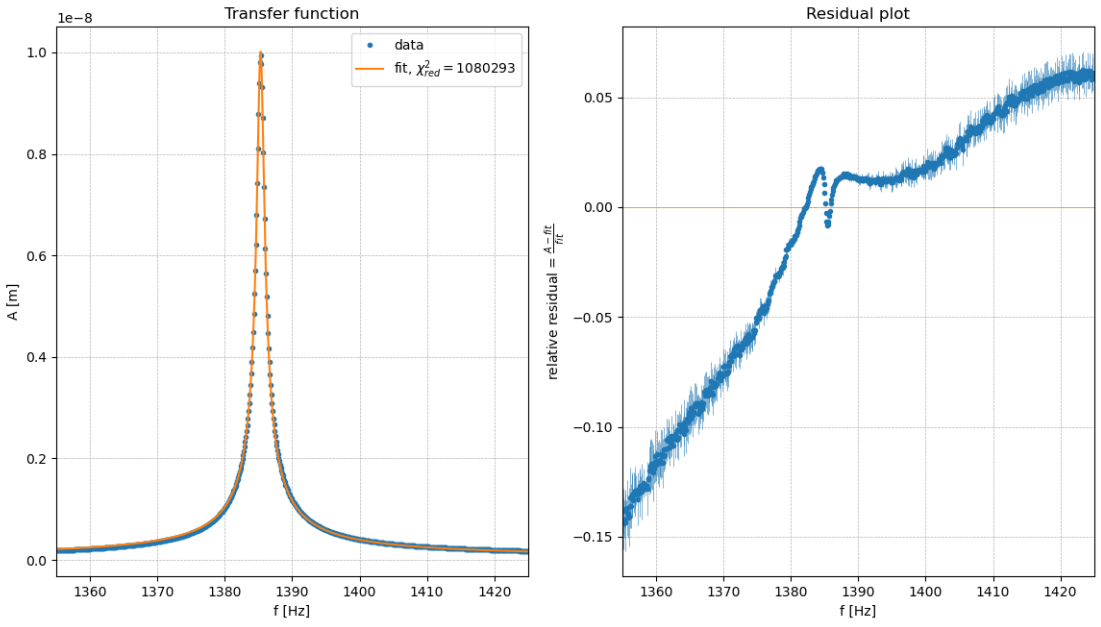

Figure 4.1: LEFT: the data of $A(f)$, the amplitude of oscillation of x, in function of the frequency of the applied potential f. The data are fitted by (4.9). The parameters of the fit are $\nu_0 = (1385.3 \pm 0.1)\text{Hz}$, $w = (1.076 \pm 0.002)\text{Hz}$, $A_{top} = (7.75 \pm 0.01)10^{-12}\text{m}$ and $c = (3.3 \pm 0.1) \cdot 10^{-11}\text{m}$; the FWHM is 1.88Hz while $Q = 739$. RIGHT: the residuals of the fit divided by the value of the fit function at the given frequency are plotted. With 697 degrees of freedom, the reduced χ^2 results very high, i.e. $\chi^2_{red} = 1.1 \cdot 10^6$. A clear behavior of the residuals is visible, verifying the limitations of the used model indicated by the high χ^2_{red}.

4.2 Thermal noise in thermodynamic equilibrium

We now show the results of an estimation of thermal noise for the longitudinal mode of vibration of the oscillator performed by the quadrature phase differential interferometer. It is performed in thermodynamic equilibrium, i.e. with the oscillator held at a fixed homogeneous temperature (297 K). The pressure reached in the vacuum chamber is $8.10 \cdot 10^{-6}$ mbar.

Following the procedure described along chapter 3: first we acquire the data from the four photodiodes to estimate the calibration ellipse (see figure 3.3, in which the data are the same ones considered here) and to compensate the photodiodes outputs (see figure 3.4); this is performed providing to the actuator sustaining the reference mirror of the Michelson interferometer a 1-Hz sinusoidal signal with peak-to-peak amplitude of 180 V and offset half such amplitude. Then (without providing the voltage to the actuator) we acquire data for 3 hours and we carry out the spectral analysis, providing the PSDs of the relative displacement ΔL for the various sets of 20 consecutive 10 s intervals of data (see figure 3.5). From all the 10 s intervals we use only those with a low enough noise floor around the frequency of the longitudinal peak, i.e. the $\nu_0 = 1385,30$ Hz found in the previous section 4.1. To this purpose, we individuate a frequency interval near the frequency of the peak in which the noise results flat and we estimate the noise floor with the mean of the PSD in such interval. In figure 4.2 left there is an example PSD coming from the average of 20 consecutive 10 s intervals, zoomed in a frequency range near the frequency of the thermal noise peak; the latter is visible at 1385 Hz, while the peak-free range 1305÷1335 Hz has been chosen to estimate the noise floor. In the right figure there is the histogram of the noise floor values for all the 10 s intervals acquired, normalized over the minimum of such noise floors. The intervals accepted are those with a normalized noise floor lower than 5.5; the choice is made in order to have a noise floor low enough to be able to correctly fit the thermal noise peak.

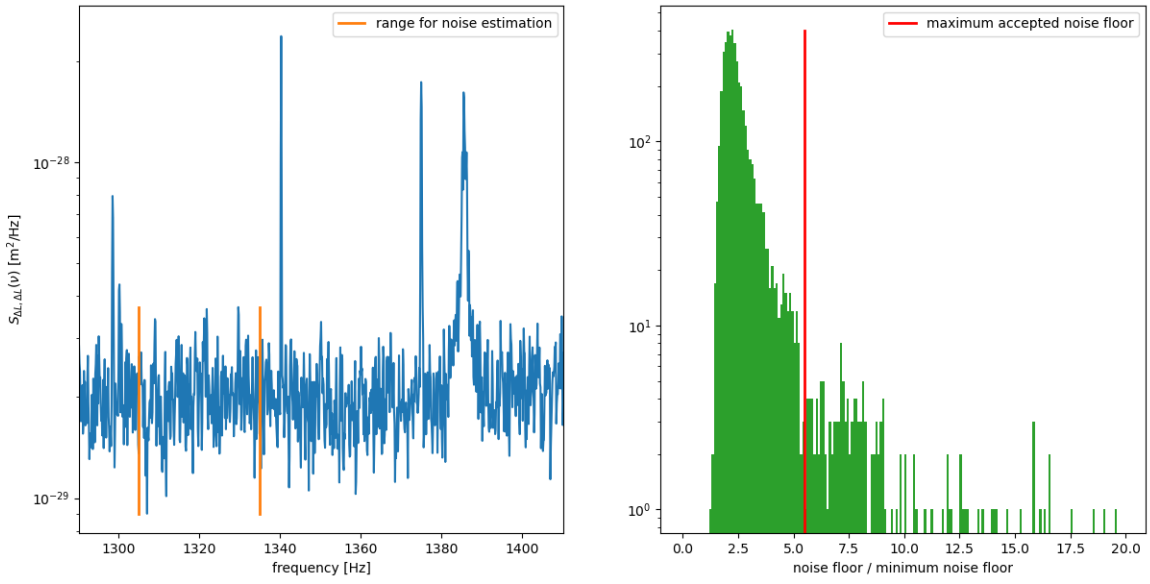

Figure 4.2: LEFT: example PSD averaged over 20 consecutive 10 s intervals zoomed near the thermal noise peak at 1385 Hz. The range 1305÷1335 Hz, having a PSD without evident peaks, is chosen to estimate the noise floor via the mean of the PSD. RIGHT: histogram of the normalized noise floor of all the 10 s intervals. Only those with a normalized noise floor lower than 5.5 are accepted.

In the PSD of ΔL, at the longitudinal resonance frequency ν_0 of the oscillator, the contribution due to the longitudinal mode of vibration due to thermal noise is observable. In figure 4.3 there are example data, coming from the average on 20 accepted intervals of measures. In accordance with the formula (1.12) for thermal noise, using the same approximation explained for formula (1.33), the

longitudinal thermal peak can be fitted by the Lorentzian function, i.e.

$$y(\nu) = y_0 + \frac{2}{\pi} A \frac{w}{4(\nu - \nu_0)^2 + w^2}, \tag{4.10}$$

in which y_0 represents the noise floor, ν_0 is the resonance frequency, w is the FWHM and A is the area of the peak. Following equation (1.14), this area results

$$A = \langle x_{Th}^2 \rangle = \frac{k_B T}{k}, \tag{4.11}$$

where k is estimated by $m\omega_0^2$, with $\omega_0 = 2\pi\nu_0$ and m the mass of the cubic mass of the oscillator. So, A provides a measure of the mean square displacement x of the oscillator from its equilibrium position due to thermal noise, displacement that is related to the temperature of the oscillator, which thus can be estimated:

$$T_{eff} = \frac{m\omega_0^2}{k_B} A, \tag{4.12}$$

where T_{eff} is for effective temperature.

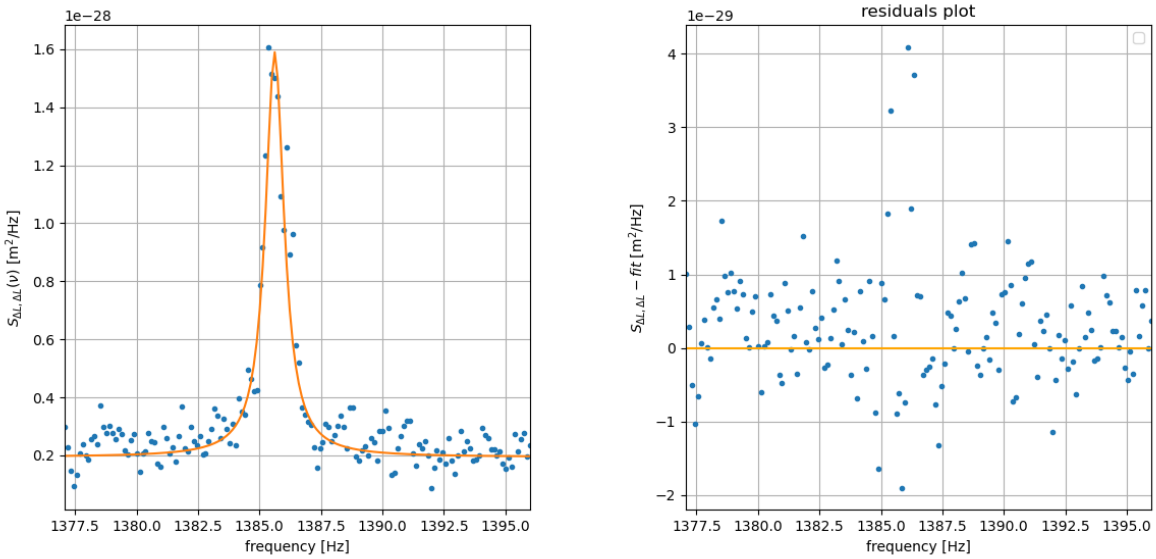

Figure 4.3: Example PSD from 20 consecutive 10 s intervals zoomed around the thermal noise peak, which is fitted by the Lorentzian function (4.10).

From every PSD coming from the average on 20 accepted intervals of measures, the data are fitted by the Lorentzian function (4.10). In figure 4.4 there are the histograms of the resonance frequencies and of the parameters w coming from the fits. We estimate their values through their mean; in table 4.1 these estimates are compared with the corresponding ones coming from the measurement of the transfer function described in section 4.1. The estimates of the parameter w, expressing the losses of the oscillator and constituting the FWHM of the Lorentzian fit, result well compatible. The estimates of the resonance frequency ν_0 are compatible barely inside three error bars; while the relative difference provides the low value of 0.028%. Their difference could be realistic and due to slightly different environmental conditions, such as in temperature.

From the Lorentzian fits, the amplitude of oscillation is quantified by the area A (see eq. (4.11)), while the estimate of the temperature of the oscillator is given by (4.12), thanks to the parameters A and ν_0 of the various fits. The results are plotted in the histogram of figure 4.5, from which we estimate the temperature with the mean.

The temperature of the oscillator measured by the thermometers placed in the apparatus results 297 K, while the previous analysis has estimated the mean amplitude of thermal noise oscillation associated to a temperature $T_{eff,mean} = (242 \pm 24)$K, which (also taking into account that its uncertainty

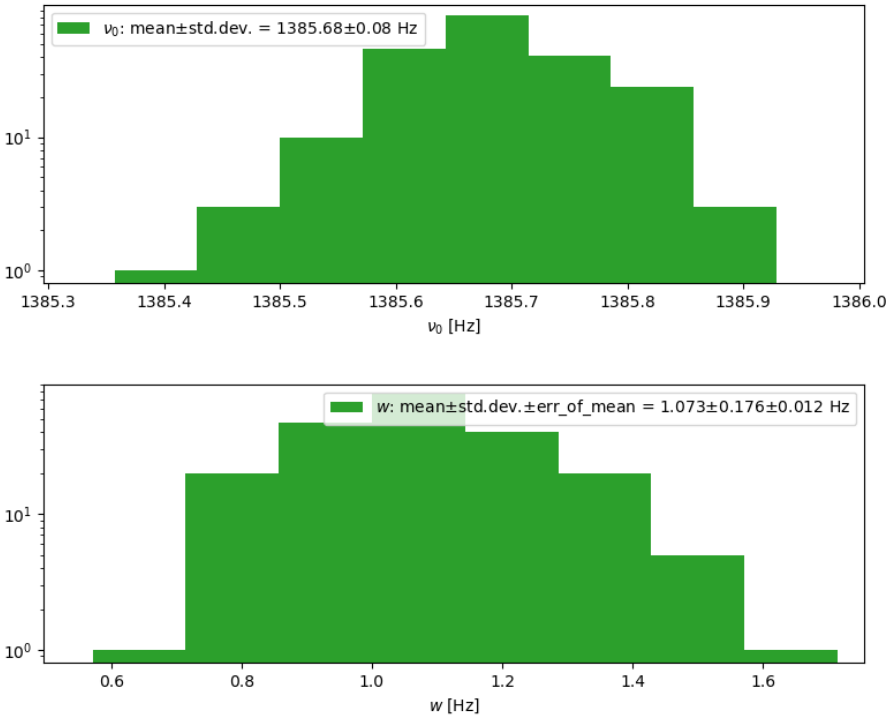

Figure 4.4: Histograms of the resonance frequencies ν_0 and the parameters w (corresponding to the FWHM of the Lorentzian function) coming from the fits of the thermal noise peak in the PSDs. Their value is estimated with the mean. The error of ν_0 is estimated by the standard deviation, because of the dependence of its distribution on the fluctuations of the conditions of the system, such as in temperature.

type of estimation:	transfer function	thermal noise peak	relative difference
ν_0 [Hz]	1385.3 ± 0.1	1385.68 ± 0.08	0.028%
w [Hz]	1.076 ± 0.002	1.073 ± 0.012	0.28%

Table 4.1: Estimates of the resonance frequency ν_0 and of the parameter w coming from the measurement of the longitudinal transfer function of the oscillator (see section 4.1) and from the thermal noise peak in the PSD of the displacement of the oscillator due to the longitudinal mode of vibration. The uncertainty on the thansfer function estimates are omitted because they result underestimated. The relative difference is the difference between the estimate from the transfer function and of the thermal noise analysis divided by their mean value.

is the conservative choice of the standard deviation) is not well compatible with 297 K. This underestimation of the effective temperature was already observed in past measurements, and it constitutes an actual limit of our apparatus. Similar problems of constant wrong estimations were present also in the previous capacitive readout (see section 1.4), as well as in various other experiments for the measurements of thermal noise. A kind of "solution" which in these cases can be applied, is to use the estimation of thermal noise in thermodynamic equilibrium to calibrate the measuring apparatus, and use it to study the conditions out of equilibrium. Anyway, this is not an ideal condition, because you can not be sure about the correct interpretation of the estimations, both out and in thermodynamic equilibrium.

In front of this limit of the apparatus, different hypotheses can be formulated. One asks if the measuring apparatus provides correct measurements of the displacement of the oscillator, or if it introduces systematical deviations in its estimates. This can be investigated by checking the calibration of the readout in different conditions. Efforts of this kind will be described in the following sections of this chapter. In section 4.3 the calibration ellipse (see section 3.2) will be estimated with different methods, to check if the way in which the interferometer is calibrated influences the result of the estimation. In section 4.4 we will make the interferometer measure known displacements in order to

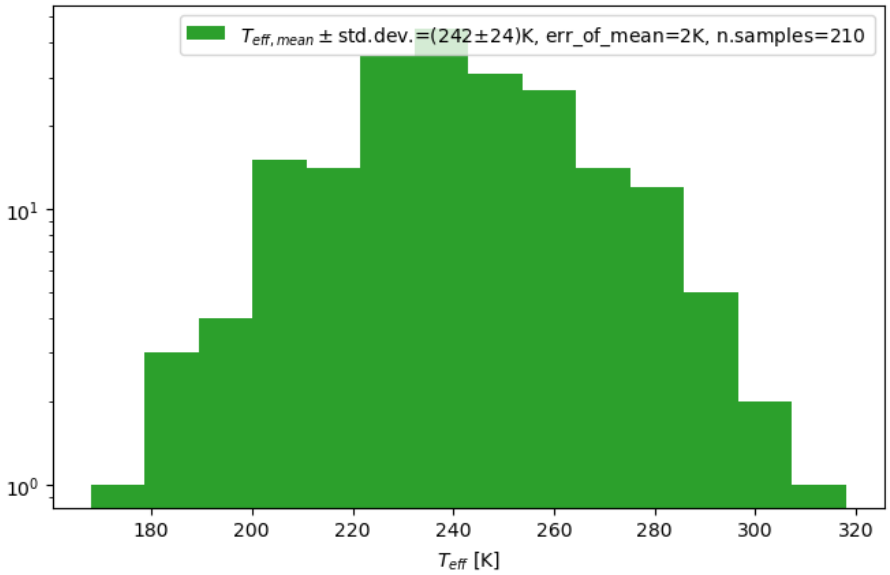

Figure 4.5: Histogram of the effective temperatures T_{eff} estimated via the thermal noise measurement. The error of the mean of 2 K is underestimated as estimate of the uncertainty of T_{eff}, because of systematic errors; a conservative choice is to use the standard deviation of 24 K.

check if it provides the correct values; this will be carried out moving the reference mirror placed below the oscillator via the piezoelectric actuator on which it is mounted (see section 2.6).

Another hypothesis is that the physical quantity we measure is not the same of that we expect we are measuring, i.e. the thermal noise displacement described by equations (1.12) and (1.13). This is supported by some observations on the experimental results. Considering the last measurement performed before those shown here, always in the same conditions (in particular, with the temperature of 297 K), we obtained $T_{eff,mean} = (210 \pm 1)$K. It is evident that the underestimation is not the only characteristic of these estimates, because you have also that the value of $T_{eff,mean}$ changed between past measurements (210 K) and those previously shown (242 K). Furthermore, also the longitudinal resonance frequency ν_0 is different between the two measurements: here it resulted (1385.684 ± 0.006) Hz, while in the previous measurements it was in the range $1400 \leq \nu_0 \leq 1402$ Hz. The same happened for the parameter w of the transfer function of the oscillator (the data are collected in table 4.2). These changes of the measured quantities are not expected based on our model of the apparatus. Significant modifications implemented to the apparatus between the last two measurement campaigns consist in the addition of a piezoelectric actuator and of an absorber on the support below the oscillator, support which is sustained by two protrusions connected to the same structure that sustains the oscillator (see figure 2.2). If the oscillator is modeled as acting as an isolated one, its thermal noise vibrations are not expected to be influenced by these two upgrades. Since the experimental evidences pointed out above show clear changes of the dynamics of the oscillator, a natural hypothesis is that the oscillator does not act as an isolated one, as assumed; so that the addition of the actuator and of the absorber causes a change of the measured physical quantities of the oscillator dynamics. In this case, the underestimation of the temperature by T_{eff} would be explained by the fact that we are measuring a displacement of the oscillator different from that described by the formulas (1.12) and (1.13) (used to relate the displacement to the temperature).

4.3 Calibration with different methods

In the end of the previous section we described the main issues of our experiment, that are the underestimation of the thermal noise vibrations and changings between different measurement campaigns for measured quantities which should not change after the applied modifications. As a way to

	past measurement campaign	present measurements
$T_{eff}[K]$	210 ± 19	242±24
ν_0 [Hz]	1400÷1402	1385.68±0.08
w [Hz]	0.61 ± 0.01	1.073 ± 0.012

Table 4.2: The results of the previous measurement campaign (that is before the changes implemented to the apparatus described in section 2.6) from the thermal noise estimation are shown together with those of the measurements described in this section. The uncertainty of T_{eff} is estimated with the conservative choice of the standard deviation of the distribution of their measurements. They show clear changes without a known motivation.

check if the measuring apparatus is correctly working, here we describe a test of the procedure with which the interferometer is calibrated. This procedure is described in section 3.2 and it leads to the estimation of the parameters of the calibration ellipse and for the compensation of the photodiodes. For the calibration you need to take data by the four photodiodes of the interferometer while you vary the arm length of the reference mirror L_M or of the oscillator L_O by at least a full fringe (for the optical scheme see figure 3.1). This can be performed with various methods and, if correctly implemented, they are expected to provide analogous results. In order to assess this, we take the data for the calibration using the three following methods:

1. A sinusoidal voltage signal of 1 Hz with the large amplitude of 180 V_{pp} and offset 90 V is applied to the piezoelectric actuator sustaining the reference mirror, which therefore changes its distance from the PBS #2, i.e. L_M. The data are acquired for 30 s and each second provides a period of the same data.

2. A sinusoidal voltage signal of 30 Hz with the small amplitude of 3.5 V_{pp} is applied to the actuator sustaining the reference mirror and its offset is gradually varied with step of 1.8 V from 1.8 V to ≈180 V; so as to check the consistency of the readout for small displacements around different working points of the interferometer along the fringe. The data are acquired for 2 minutes.

3. The heater placed in the vacuum chamber is briefly switched on to heat the cubic mass of the oscillator, which therefore lengthens for thermal expansion with the consequent change of the distance of the lower surface of the oscillator from the PBS #2, i.e. L_O.

The parameters of the calibration estimated with these three methods, i.e. the parameters of the calibration ellipse and the slope of the linear fit of the compensation of the photodiodes, are reported in table 4.3.

method	1. L_M large signal	2. L_M signals varying offset	3. oscillator expansion
calibration ellipse:			
X_0	-0.0090	-0.0078	-0.0082
Y_0	0.0049	0.0060	0.0053
X	0.8913	0.8940	0.8964
Y	0.8844	0.8840	0.8841
ϕ [rad]	-0.0060	0.0010	-0.0002
photodiodes compensation:			
b_{BA}	0.988	0.987	0.991
b_{DC}	1.024	1.021	1.027

Table 4.3: Parameters of the calibration ellipses and of the fits for the compensation of the photodiodes estimated with the three methods described in the text. The calibration is described in section 3.2, where the parameters of the ellipse are defined in equations (3.22) and (3.23) while the fit function of the compensation of the photodiodes (for the A and B ones) is defined by equation (3.32).

In order to evaluate the importance of the (slight) differences between the calibration parameters coming from the various methods, these parameters are used for an estimation of thermal noise, similar to that shown in section 4.2 (only with less data, because part of the data were rejected for problems

during the data taking), using the same raw data for all the three calibrations. The resulting estimates of T_{eff}, ν_0 and w are shown in table 4.4 and they are also plotted in figure 4.6. These estimates are well compatible between the various calibration methods, always well within one error bar, and also their uncertainties have similar values. In conclusion, we find no evidence of an issue with any of these calibration methods that could explain the observed discrepancy in the measured effective temperature at equilibrium.

calibration method	T_{eff} [K]	ν_0 [Hz]	w [Hz]
1. L_M large signal	246.9 ± 4.3	1386.090 ± 0.017	1.351 ± 0.032
2. L_M signals varying offset	248.3 ± 4.5	1386.092 ± 0.015	1.339 ± 0.030
3. oscillator expansion	246.0 ± 4.4	1386.090 ± 0.018	1.362 ± 0.033

Table 4.4: Estimates of T_{eff}, ν_0 and w from the analysis of the same raw data (of 50 minutes) performed three times, using calibration parameters estimated with three different methods. (These estimates are not simply confrontable with those shown in table 4.2 of the previous section because of differences of temperature and pressure in the vacuum chamber.)

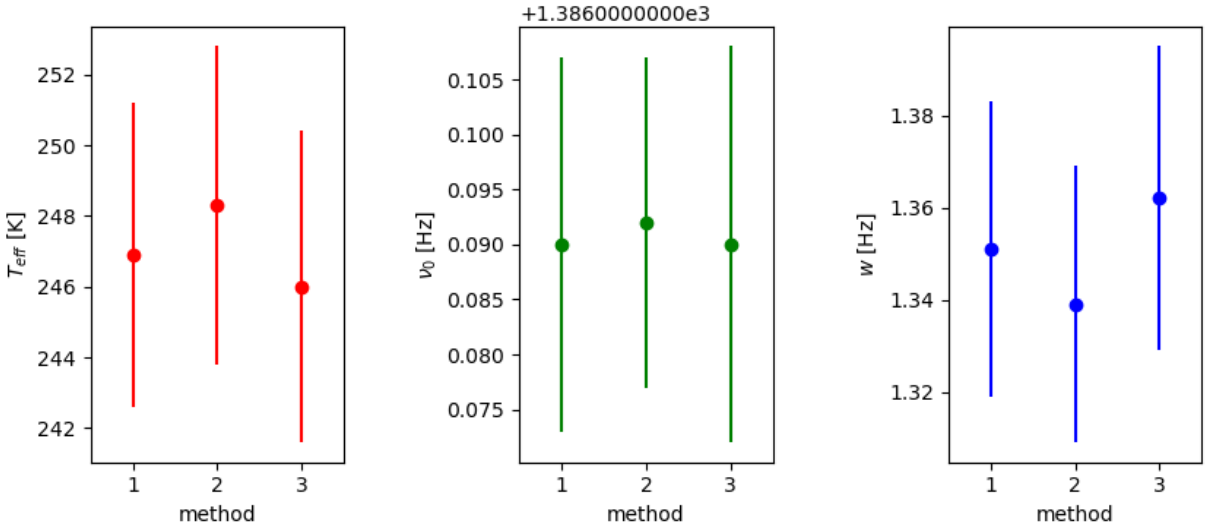

Figure 4.6: The estimates obtained using the three different calibration methods of table 4.4, i.e. the effective temperature T_{eff}, the resonance frequency ν_0 and the parameter w, are plotted. The graphs clearly show the compatibility of the estimates among the different methods.

4.4 Calibration with piezoelectric actuator

The calibration methods discussed in section 4.3, and shown to provide equivalent results, are intended to correct non-linearities and other non-ideal behaviors of the interferometer's components. However they are self-referenced. Here instead, we want to check the interferometer response to externally controlled signals. This is carried out providing a known displacement to the reference mirror below the oscillator via the piezoelectric oscillator on which it is mounted (for the optical scheme see figure 3.1) and measuring such displacement with the interferometer; from the comparison of the known magnitude of the displacement with that estimated by the interferometer we can evaluate its accuracy. For this purpose, we need an accurate characterization of the piezoelectric actuator, in particular of its displacement when a certain voltage signal is applied; a characterization that has to be achieved without using the quadrature phase differential interferometer. The voltage-dependent displacement curves of a piezoelectric actuator are nonlinear and subject to hysteresis [17]. Moreover, they have drift dynamics (creep) when a fixed potential is applied. So, our characterization take in consideration specific voltage signals applied to the actuator, the same signals that then will be used to calibrate the quadrature phase differential interferometer. The chosen specific signals are AC ones, of sinusoidal type; this choice is motivated by the fact that in this way we are able to provide to the

interferometer displacements similar (at least for certain properties, such as frequency and shape) to that due to thermal noise.

4.4.1 Calibration of the piezoelectric actuator

Before mounting the piezoelectric actuator in the apparatus, we studied its response to AC voltage signals. The actuator is placed in a Michelson interferometer and it sustains one of its two mirrors (see figure 4.7), so that a displacement of the actuator changes the interference condition. This apparatus is simpler than the quadrature phase differential interferometer previously described (see chapter 3), both in optical layout and in data analysis, so that we can be more confident on its estimations.A displacement of the actuator changes the interference condition, with the power detected by the photodiode described by the formula

$$P = P_0(1 + \mathcal{V}\cos\Delta\phi) = P_0(1 + \mathcal{V}\cos(\Delta\phi_0 + k2x)), \tag{4.13}$$

where $\mathcal{V}$ is the visibility of the fringes, $\Delta\phi$ is the phase difference between the two interfering beams, $\Delta\phi_0$ is the phase difference without changing the length of the actuator, $k = \frac{2\pi}{\lambda}$ is the wave number of the laser (with $\lambda = 1064$nm) and x is the displacement of the actuator from its length at rest, that is in function of the voltage applied to it.

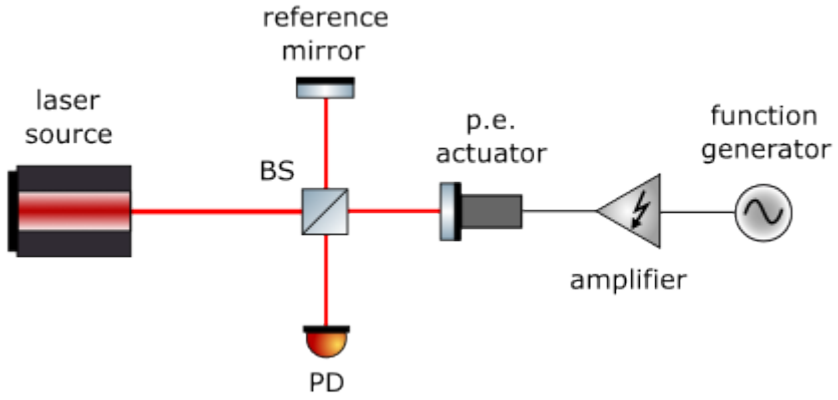

Figure 4.7: Scheme of the Michelson interferometer. The beam comes from the laser source and it is splitted by the beam splitter; the two beams are reflected by the reference mirror and the mirror mounted on the piezoelectric actuator back to the beam splitter that reflects half of the power of the two beams into the photodiode, where they recombine and interfere. A function generator followed by an amplifier provides high voltage signals to the piezoelectric actuator. Both the output of the photodiode and the voltage provided by the amplifier are measured.

A first calibration is performed applying to the actuator AC voltage signals with high amplitudes, able to lead the interference through various fringes for each period of the voltage. In figure 4.8 there are the raw data associated to one period of a sinusoidal applied signal with peak-to-peak voltage $V_{pp} = 535$V and frequency 1Hz. The voltage signal provided by the photodiode is plotted in function of the applied voltage, that is measured too. The blue points belong to the phase in which the applied voltage increases, while the orange points belong to the subsequent phase in which the applied voltage decreases. If there would be a fixed relation between the applied voltage V and the displacement of the actuator x, the blue and orange points would overlap; but this is not the case: the data show a hysteresis. This means that the conversion factor between the applied voltage and the displacement of the actuator, defined by

$$C = \frac{dx}{dV}, \tag{4.14}$$

changes with the changing of the applied voltage along a period, and moreover it changes in different ways between the half period in which the applied voltage increases with respect to that in which it decreases.

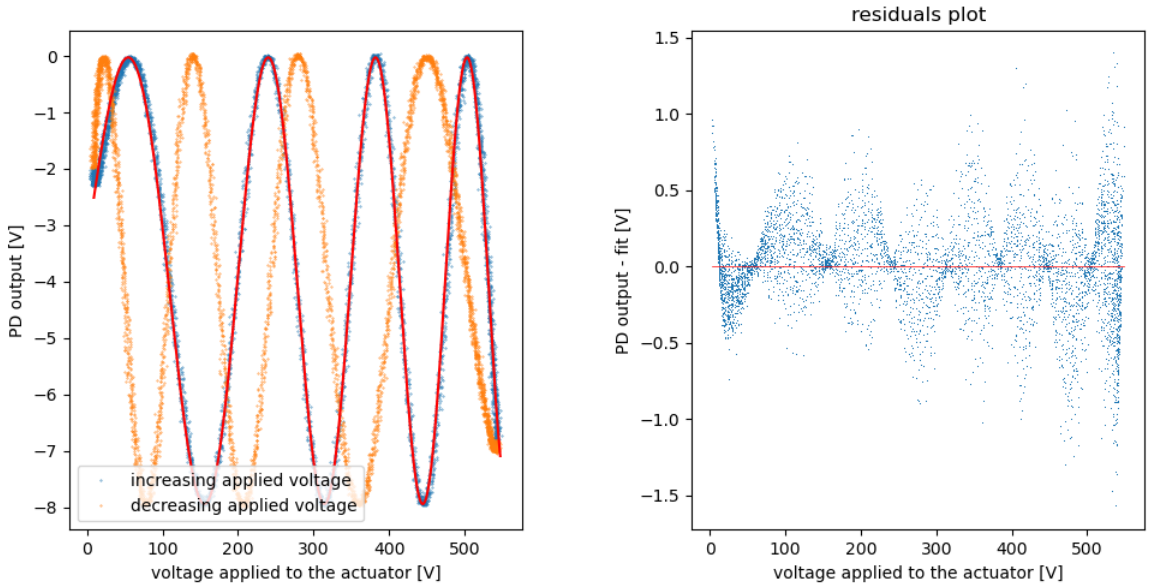

Figure 4.8: Example data of the voltage signal provided by the photodiode of the Michelson interferometer in function of the measured voltage applied to the piezoelectric actuator. The latter has a peak-to-peak amplitude of 535V and a frequency of 1Hz. The data are divided in those in which the applied voltage is increasing (blue) and those in which it is decreasing (orange). The data with the voltage which is increasing are fitted with the formula (4.13) assuming a conversion factor varying as a second degree polynomial, that is by the function $y = p_0 + p_1 \cos(p_2 + p_3 V + p_4 V^2 + p_5 V^3)$. In the right graph the residuals are plotted. The visible periodical structure is due to the fact that when the absolute value of the fit slop increases, the fluctuation of the data in the x variable causes a higher effect on the residual value, which is in the y variable, an effect that is expected proportional to such slope. Considered this, since along the x axis the residuals are quite symmetrically distributed around the null value, their distribution is that expected for a good fit.

In a period of a sinusoidal voltage applied to the actuator, when the voltage increases also the conversion factor increases, and just when the voltage starts to decrease the conversion factor assumes its minimal value and then increases while the voltage decreases. We directly fit the interferometer data with equation (4.13), assuming a conversion factor C quadratic in the applied voltage, which gives a displacement:

$$x = a + bV + cV^2 + dV^3. \tag{4.15}$$

The corresponding conversion factor is given by

$$C = \frac{dx}{dV} = b + 2cV + 3dV^2, \tag{4.16}$$

where in the last passage equation (4.15) is used. In figure 4.8 there is an example of the fit of the data, providing an estimate of the conversion factor through equation (4.16). Both for the data with the applied voltage increasing and those with the applied voltage decreasing, this estimate is repeated for 10 consecutive periods of the applied voltage, and a final estimate is provided by the mean the 10 provided functions, which consists in the mean of their parameters. In figure 4.9 this final estimate of the conversion factor is plotted for sinusoidal voltage applied to the actuator with different frequencies. With a higher frequency, the conversion factor becomes lower.

A second calibration is performed by applying to the actuator sinusoidal voltages with small amplitudes and the high frequencies of 1410 Hz and 320 Hz, in order to have signals with properties similar to those due to thermal noise; in particular, the first longitudinal mode of vibration excited by thermal noise (see figure 1.8) has a frequency of ≈1400 Hz, while the first transverse mode of ≈320 Hz. In this case, the just described varying of the conversion factor along a period of the applied voltage becomes negligible and the conversion factor is considered constant. In the left graph of figure 4.10 there is an example of raw data (blue and yellow points) with the applied voltage with $V_{pp} = 3.6$V

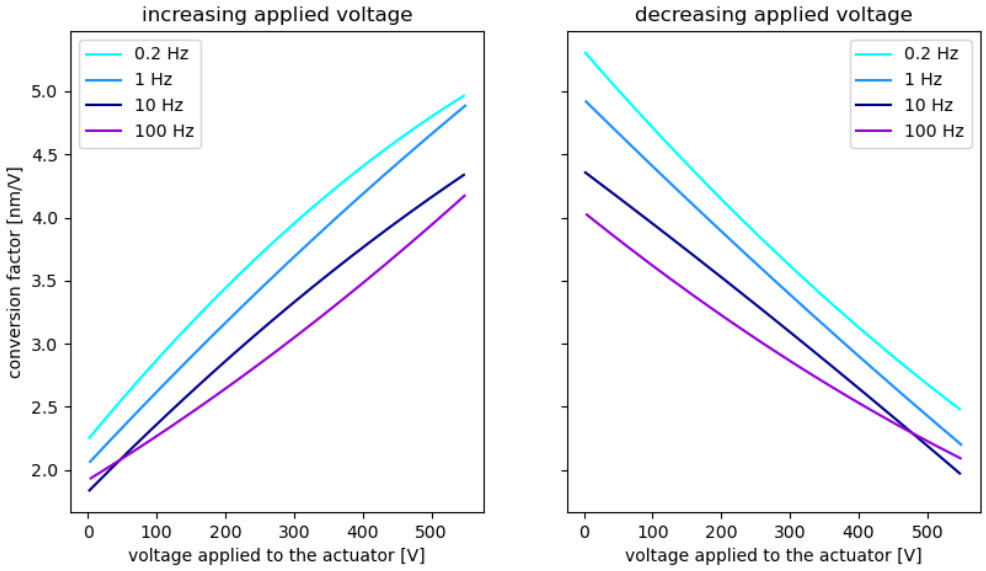

Figure 4.9: Conversion factors associated to an applied voltage with $V_{pp} = 535$V and offset of half the peak-to-peak amplitude, to maintain the applied voltage monopolar at all times. They are estimated assuming a second degree polynomial dependence on the applied voltage and they are the averages over 10 estimates (i.e. functions $C = C(V)$ given by eq. (4.16)) coming from 10 consecutive periods. The left graph shows the conversion factor when the applied voltage increases, while the right graph when the applied voltage decreases. The estimates are provided for 4 frequencies of the applied voltage, for which the reduction of the conversion factor with the increase of the frequency is observable.

and frequency of 1410Hz. The visibility of the interferometer has been estimated, via separate specific measurements, and the estimates of the minimum and maximum of interference, which are the minimum and maximum of formula (4.13), are also plotted (red and green lines). The displacement of the actuator is obtained from the photodiode output inverting formula (4.13), obtaining (unless an offset):

$$x = \frac{1}{2k} \cos^{-1}\left(\frac{P_{PD} - P_{PD,0}}{P_{PD,0}\mathcal{V}}\right), \tag{4.17}$$

where P_{PD} and $P_{PD,0}$ are the outputs of the photodiode corresponding to the measured powers P and P_0 of formula (4.13), and, thanks to the measured maximum $P_{PD,max}$ and minimum $P_{PD,min}$ photodiode output (corresponding to the minimum and maximum of the interference fringes respectively (because the output of the photodiode is negative)), they can be expressed by

$$P_0 = \frac{P_{PD,max} + P_{PD,min}}{2}, \tag{4.18}$$

$$\mathcal{V} = \frac{P_{PD,max} - P_{PD,min}}{P_{PD,max} + P_{PD,min}}. \tag{4.19}$$

The displacement of the actuator x is plotted in the right graph of figure 4.10. Now, the conversion factor can be estimated by the ratio of the amplitude of oscillation of the displacement and of the applied voltage. As visible in figure 4.10 right, in addition to the expected oscillation at 1410 Hz, the data show random fluctuations, due to the instability of the oscillation of the actuator and to the power fluctuations of the laser. Their contribution in the estimation is random, so that their contribution are reduced by the averages performed in the analysis.

The conversion factor is estimated by an average on 10 consecutive periods of oscillation of the applied voltage. This estimate is repeated with different offsets of the applied voltage and an important dependence of the conversion factor on the offset, in the range of $0 \div 180$V, has not been observed. Example data are visible in figure 4.11; their systematic deviations are not due to a dependence on the

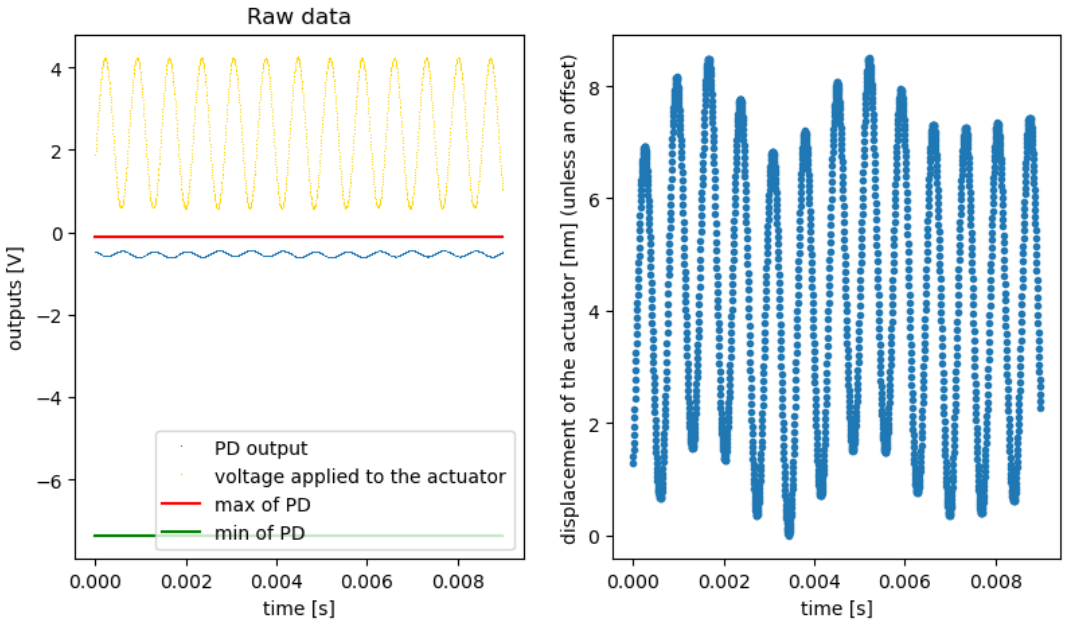

Figure 4.10: Example data with small sinusoidal voltage applied to the actuator. On the left there are the raw data and the measured maximum and minimum of the PD output, corresponding to the minimum and maximum of the interference. On the right there is the displacement of the actuator derived from the PD output. In addition to the expected oscillation at 1410Hz, due to the oscillation of the actuator, the data show an other fluctuation, a random one, due to the instability of the oscillation of the actuator and to the power fluctuation of the laser. The applied voltage has $V_{pp} = 3.6$V, offset=2.4V and frequency 1410Hz.

offset of the applied voltage, but to the estimation method, in particular to the inaccuracy in the estimation of the maximum of the photodiode output (corresponding to the minimum of the interference). From the estimates at various offsets you obtain a mean conversion factor. This estimation is repeated various times in different days in order to investigate the constancy of the response of the actuator and the results are shown in figure 4.12. They are related to a small sinusoidal signal applied to the actuator with $V_{pp} = 3.6$V and the two frequencies of 1410 Hz and 320 Hz. Final conversion factors can be estimated by the averages $C_{1410Hz} = (1.96 \pm 0.04)$nm/V and $C_{320Hz} = (1.74 \pm 0.03)$nm/V.

4.4.2 Calibration of the quadrature phase differential interferometer

The piezoelectric actuator characterized in the previous subsection is now placed in the apparatus and it sustains the reference mirror, so that it can be used to calibrate the quadrature phase differential interferometer. For this purpose, we carry out measurements in the same conditions of those performed outside the apparatus for the calibration of the actuator.

Now, with the quadrature phase differential interferometer, we exploit the procedure described in sections 3.1 and 3.2 which provides the relative displacement ΔL, of which the main contribution is provided by the movement of the reference mirror induced by the actuator. So, such procedure can be tested. Another difference is that we don't acquire the voltage applied to the actuator at the same time in which we measure the data of the four photodiodes needed to reconstruct ΔL, because of the limited number of channels of the acquisition system. However, this is not a problem because we have verified the precision and the stability of the voltage signal provided to the actuator, so that we will be able to reliably estimate its value.

Analogously to the characterization of the previous subsection, the first type of voltage signals used is a sinusoidal one with the large amplitude of 532 V_{pp} and offset of half the peak-to-peak amplitude, with the frequencies of 0.2, 1, 10 and 100 Hz. For each of these signals at different frequencies, the

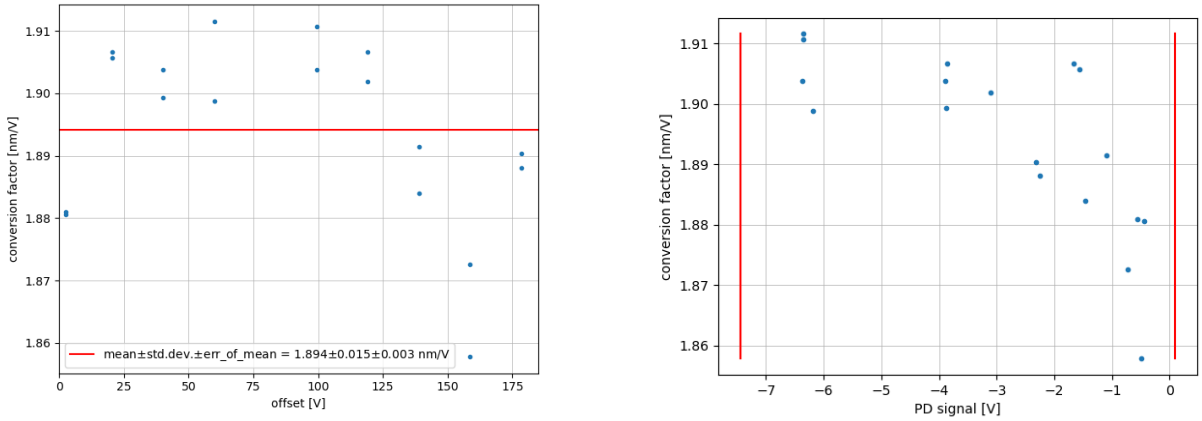

Figure 4.11: LEFT: Example conversion factors estimated with the applied sinusoidal voltage with the small amplitude of 3.6 V_{pp} and frequency of 1410 Hz. The estimates have been provided with different offsets for the applied sinusoidal potential, with two estimates for every considered offset. RIGHT: the conversion factor are plotted in function of the mean photodiode output of the raw data from which they are estimated, with the vertical lines which are the minimum and the maximum of the photodiode output due to the interference. The estimates show a clear systematic deviation for estimates near the maximum of the photodiode output, i.e. toward the right of the graph.

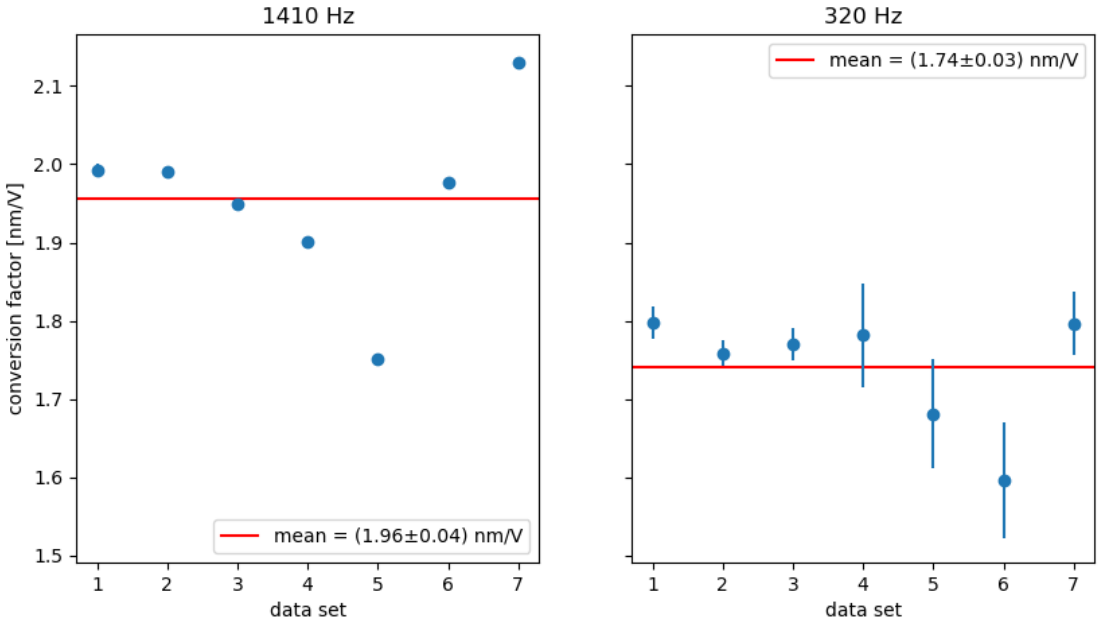

Figure 4.12: Estimates of the conversion factor for small sinusoidal voltages applied to the actuator, with $V_{pp} = 3.6$V and frequency 1410Hz (left) and 320Hz (right). Each estimate comes from an average on conversion factors estimated with different offsets of the applied voltage. The various average estimates come from different data taking in different days and they are plotted in temporal order.

applied voltage V is measured and it is fitted by the sinusoidal function

$$V = a + b\cos(ct + d), \tag{4.20}$$

where t is the time. In figure 4.13, fitted example data are shown. This relation will be used to estimate the voltage applied to the actuator at a given time.

For each signal of a certain frequency, we acquire the data for the measure of ΔL; in figure 4.14 left, example data of ΔL for the frequency of the applied voltage of 1 Hz are plotted as a function of

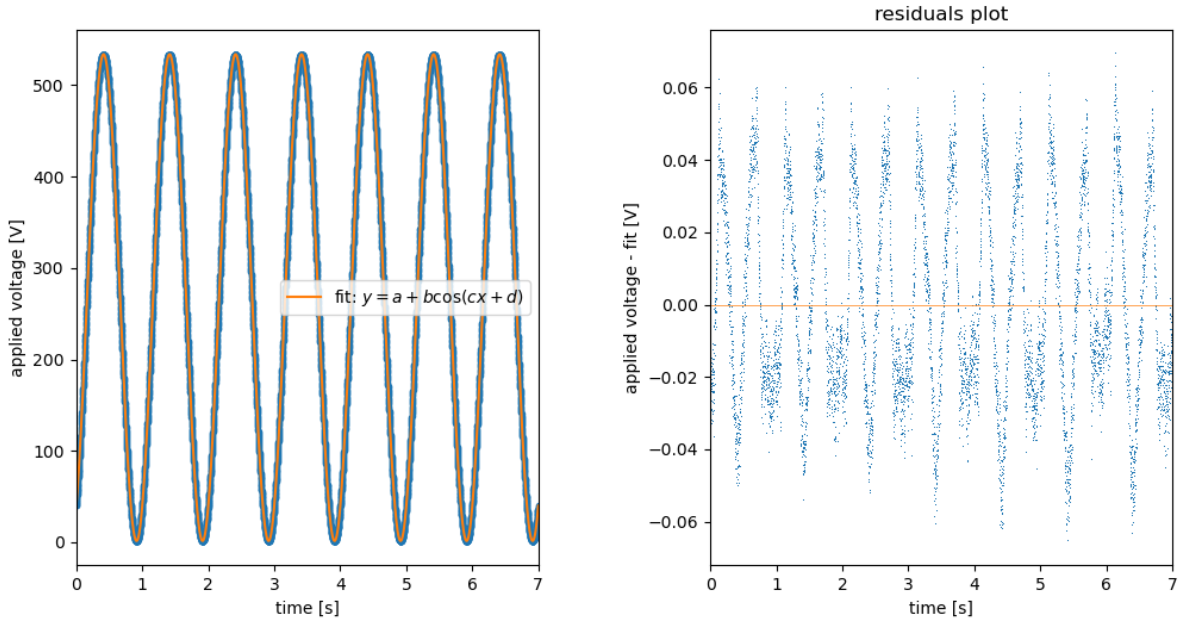

Figure 4.13: Example data of the voltage applied to the actuator, with the applied signal with the frequency of 1 Hz. The data are fitted by the function (4.20). The residuals in the right graph are small compared to the amplitude of oscillation, with a ratio in the order of 10^{-4}.

time. Now, the relation (4.20) is used to substitute the temporal x coordinate with the corresponding voltage that is applied to the actuator at a certain time (exploiting that a minimum of ΔL coincides with a minimum of the applied voltage). The resulting data are plotted in figure 4.14 right for one period, which is composed by a half period in which the applied voltage increases (blue points) and by a half period in which the applied voltage decreases (orange points).

Now, the position of the actuator, expressed by ΔL, is plotted in function of the applied voltage; so, with the same purpose of the previous subsection of estimating the conversion factor from applied voltage to displacement of the actuator, these data are fitted by an appropriate relation. Previously, the conversion factor was estimated assuming a second degree polynomial relation with the applied voltage (see figure 4.9); the same choice can not be repeated here, in fact the resulting residuals of the fit (for the half period in which the applied voltage increases) are those shown in figure 4.15 left, which show clear systematic deviations from the fit function. So the data are fitted assuming a third degree polynomial relation with the applied voltage, i.e. with a fourth degree polynomial relation of ΔL with the applied potential:

$$\Delta L = a + bV + cV^2 + dV^3 + eV^4. \tag{4.21}$$

The residuals are shown in figure 4.15 right and they show a better agreement of the data with the fit with respect to the fit performed with a third degree polynomial function, of which the residuals are shown in figure 4.15 left. In particular, both the residuals show an oscillating behavior, but in figure 4.15 right the oscillations are quite around the null value, while in figure 4.15 left an additional less frequent and with a higher amplitude oscillation is present. The fit is also plotted in figure 4.14 right.

In accordance with the definition given by (4.14), the conversion factor C can be estimated from the fit function through the relation

$$C = \frac{d(\Delta L)}{dV} = b + 2cV + 3dV^2 + 4eV^3, \tag{4.22}$$

where for the last passage the relation (4.21) is considered. This fit is repeated for 10 consecutive periods of data and a final estimate is provided by mean of their functions, which consists in the mean of their parameters. The results, for all the four applied voltages with different frequencies, are shown

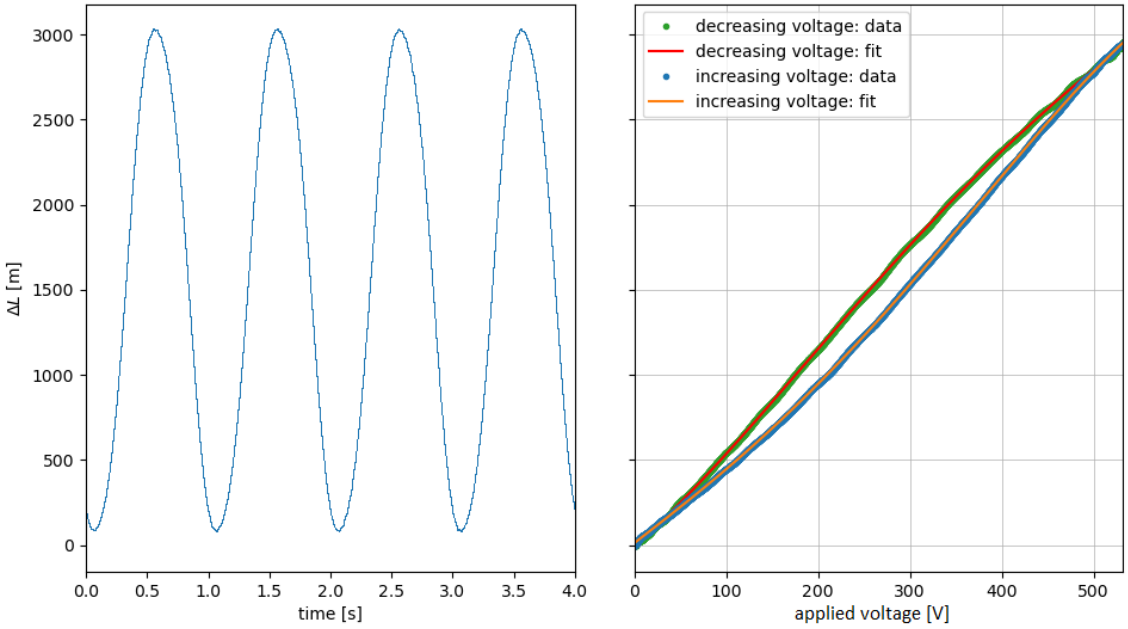

Figure 4.14: Example data for ΔL with the voltage signal applied to the actuator with frequency of 1 Hz. To the left, ΔL is plotted in function of the acquisition time. To the right, ΔL is plotted for one period in function of the applied voltage estimated exploiting the fit shown in figure 4.13. The data are divided between those in which the applied voltage is increasing (blue points) and those in which it is decreasing (orange points). These data are fitted with the function (4.21) for both the two half period of data (the residuals, for the case in which the applied voltage increases, are shown in figure 4.15), i.e. assuming a third degree polynomial dependence of the conversion factor on the applied voltage.

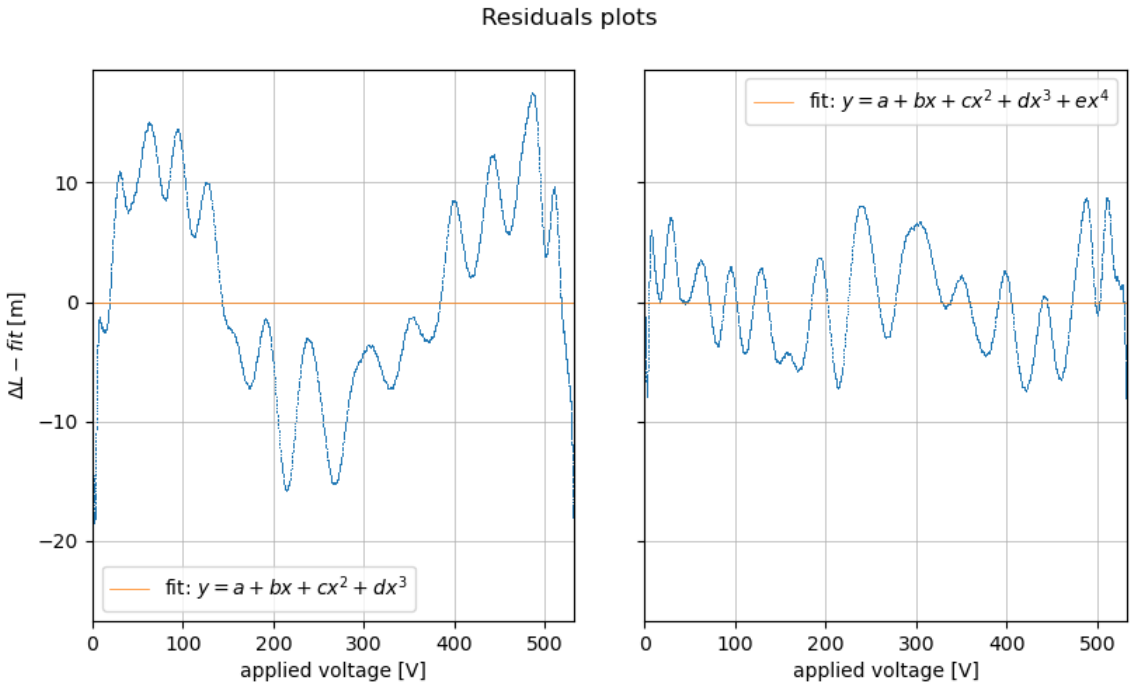

Figure 4.15: The residuals of the fit for the example data of figure 4.14 right in which the applied voltage is increasing. To the left the fit assumes a third degree polynomial dependence of ΔL on the applied voltage (with the related second degree polynomial dependence of the conversion factor), while to the right a fourth degree polynomial one (i.e. equation (4.21)).

in figure 4.16. These graphs must be compared to those of the previous characterization outside the quadrature phase differential interferometer shown in figure 4.9. If the actuator has been moved in the

same way and the measuring apparatuses have worked correctly, they should be compatible between each other, which is not the case. It is also worth to noting that the results of the previous subsection could be provided assuming a second degree polynomial conversion factor, while in this subsection such a relation was not able to describe the conversion factor, that was estimated with a third degree polynomial function. Finally, the results in figure 4.16 are generally much higher than those in figure 4.9. This is quantified and shown in figure 4.17, where the mean conversion factor over a half period of the applied voltage of the fit functions is plotted for the various frequencies and for the two measuring apparatuses. Averaging over the four frequencies and the estimates associated to an increasing and a decreasing voltage, the mean conversion factor of the second characterization is 59% higher than that of the previous first characterization. These two differences for the conversion factor between the two characterizations, both in the magnitude and in the type of relation with the voltage applied to the actuator, are not easily explainable by a wrong calibration of the measuring apparatus, but they suggest a change of behavior of the actuator from a characterization and the other; this will be confirmed by the next results.

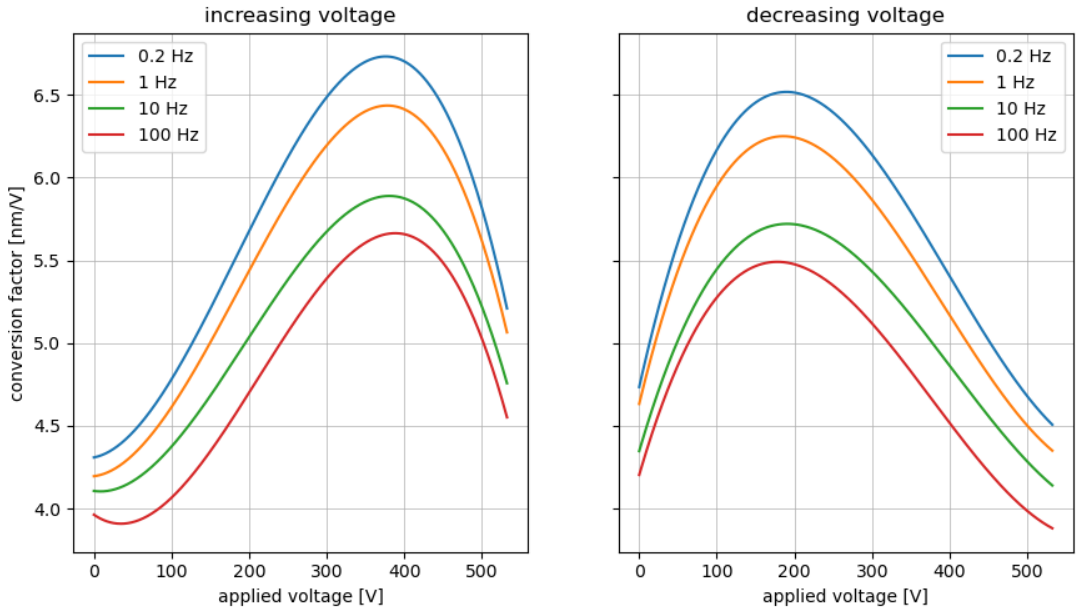

Figure 4.16: Conversion factors associated to applied voltage signals with an amplitude of 532 V_{pp} and offset of half the peak-to-peak amplitude. They are estimated assuming a third degree polynomial dependence on the applied voltage and averaging over the estimates coming from 10 consecutive periods. The left graph shows the conversion factor when the applied voltage increases, while the right graph when the applied voltage decreases. The estimates are provided for applied voltage signals with 4 different frequencies.

Analogously to the characterization of the previous subsection, the second type of voltage signals applied to the actuator for this study is a sinusoidal one with the high frequencies of 320 Hz and 1410Hz and with the small peak-to-peak amplitude of 3.5 V_{pp}. In this condition the varying of the conversion factor along a period observed in 4.16 results small compared to the value of the conversion factor, and we focus only on the mean value. The latter is estimated by the ratio of the amplitude of oscillation of ΔL, measured by the quadrature phase differentiail interferometer, and the amplitude of the applied voltage. This second amplitude, for the two frequencies of the applied voltage, is estimated by the amplitude of the sinusoidal fit on the applied voltage data (analogously to what shown in figure 4.13 for the large amplitude voltage signal case). The amplitude of ΔL is estimated fitting the data of ΔL with a sinusoid in an interval around a half period, which is used to estimate the difference of ΔL between a minimum (or maximum) and the following maximum (or minimum). An example of the fits are shown in figure 4.18. The amplitude of oscillation of ΔL is estimated for 10 periods (i.e. 20 times) and a final estimate is provided by the mean value. In figure 4.18 a drift of the 1410-Hz oscillating data is visible; such drift has the effect to increase the estimated amplitude when the fit is performed

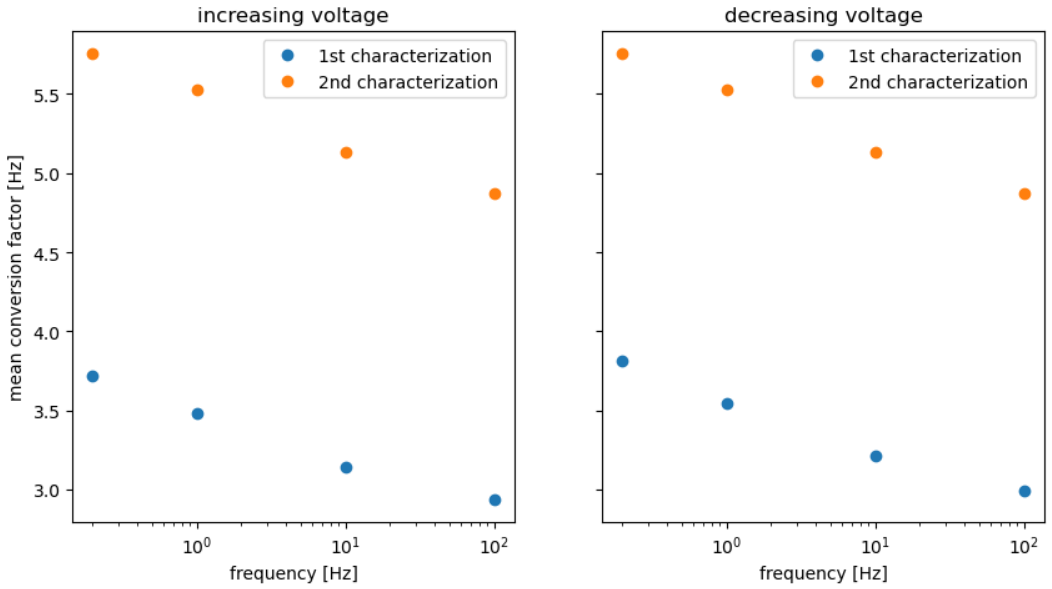

Figure 4.17: For the results shown in figures 4.16 (2nd characterization) and 4.9 (1st characterization), the mean conversion factors over a half period, for the various applied voltage with different frequencies, are plotted. To the left the estimates are referred to the half periods in which the applied voltage increases, to the right to the other ones in which the applied voltage decreases.

(in this example) from a minimum to a maximum, and to reduce it when the fit is performed from a maximum to a minimum, so that the two effects compensate.

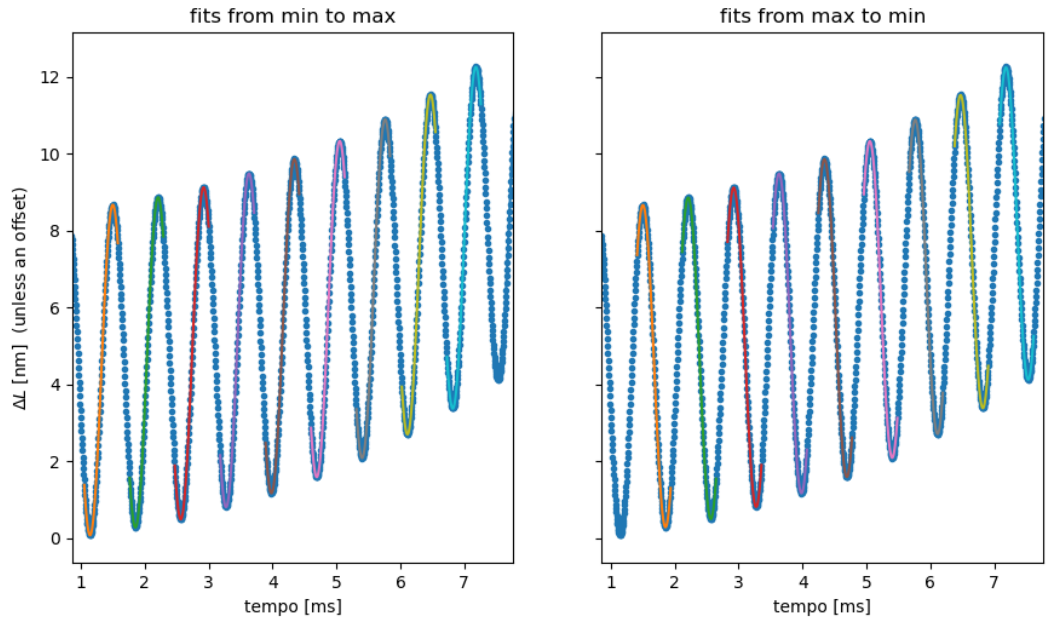

Figure 4.18: The data of ΔL are fitted by sinusoids to estimate the amplitude of oscillation for each half period of oscillation for 10 consecutive periods. To the left the fits are performed from a minimum and a maximum of the data, to the right from a maximum and a minimum. The data show a drift of the sinusoidal oscillation, increasing the amplitudes of the fits in the left graph, but reducing those of the right graph. The applied sinusoidal voltage has frequency of 1410 Hz, amplitude of 3.5 V_{pp} and offset of 2.4 V.

This kind of estimate of the conversion factor is performed with applied sinusoidal voltage with various offsets, repeating the measurement two times for each offset. The results are shown in figure

4.19. A final estimate of the conversion factor is given by the average of these estimates. These results for the two frequencies of 320 Hz and 1410 Hz are shown in table 4.5, where they are compared with the corresponding results obtained from the previous characterization (i.e. from figure 4.12). The conversion factors here estimated by the quadrature phase differential interferometer are higher than those coming from the first characterization and incompatible with them. Moreover, from the first characterization to the second one, the conversion factor at 320 Hz has increased by 1.47 nm/V, i.e. 85%, clearly more than that at 1410 Hz (of 0.37 nm/V, i.e. 19%). So much so that in the first characterization the conversion factor at 320 Hz resulted lower than that at 1410 Hz, while in this second characterization the former is higher than the latter.

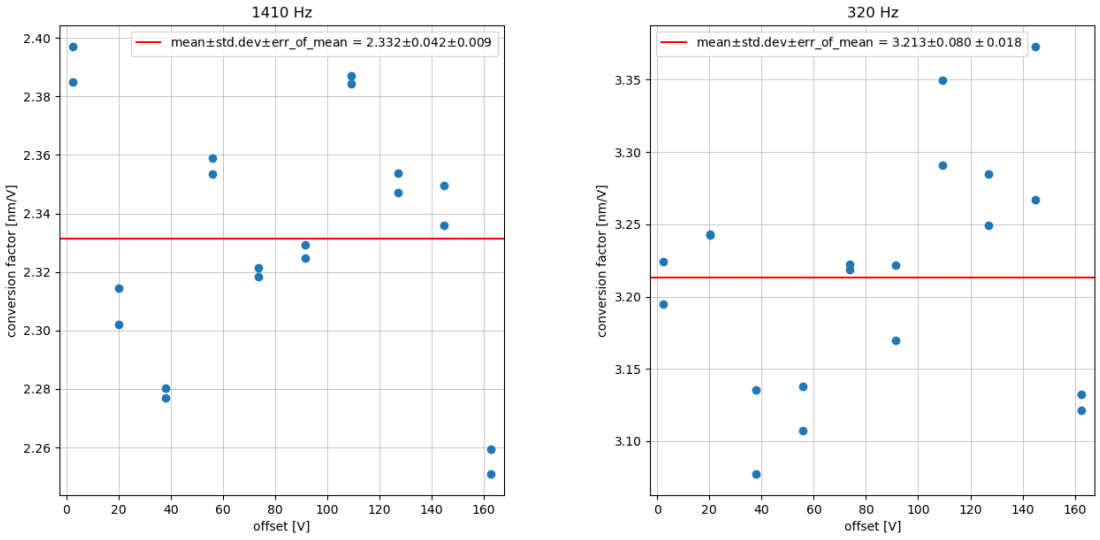

Figure 4.19: Estimates of the mean conversion factor for voltage signals applied to the actuator with the small amplitude of $3.5V_{pp}$ as function of different offsets considered. To the left the applied signal has the frequency of 1410 Hz, while to the right of 320 Hz.

characterization	1410 Hz	320 Hz
1° [nm/V]	1.96 ± 0.04	1.74 ± 0.03
2° [nm/V]	2.332 ± 0.009	3.213 ± 0.018
2° / 1°	1.19 ± 0.02	1.85 ± 0.03

Table 4.5: From both the two characterizations of subsections 4.4.1 (1°) and 4.4.2 (2°), the final estimates of the conversion factors for voltage signals applied to the actuator with the small amplitude of $\approx 3.5V_{pp}$ and the two frequencies of 1410 Hz and 320 Hz. The last line shows the ratio between the estimates coming from the second characterization and the first one.

This result is not easily explainable hypothesizing a wrong calibration of the apparatus. In particular, if the quadrature phase differential interferometer were really overestimating the displacements of the reference mirror moved by the actuator, it is expected that it overestimates the oscillation at 1410 Hz and at 320 Hz in a similar way, which is not the case. Moreover, the hypothesis of wrong calibration would lead to state that the quadrature phase differential interferometer overestimates the measured displacements, but this is in contrast with the estimations of thermal noise (described in section 4.2), which underestimate the displacements. So, the more plausible way to explain the changes of the conversion factors is with a change of working of the actuator between the two characterizations. To clarify this situation, further investigations are needed.

Chapter 5

Conclusions

In this thesis, an experimental apparatus dedicated to the study of thermal noise, as vibrations of a mechanical oscillator, has been described. The oscillator can be studied both in and out thermodynamic equilibrium, that is with a stable temperature gradient. The oscillator displacement is measured by a quadrature phase differential interferometer.

In the past measurements the apparatus had underestimated the thermal noise vibrations. So here further measurements and investigations were performed. The transfer function of the oscillator for vertical excitations has been measured, finding in this way the longitudinal resonance frequency, i.e. the same frequency at which the thermal noise vibration of the longitudinal acoustic mode is expected and which is needed for its estimation. Then, a measurement of thermal noise in thermodynamic equilibrium has been described. The estimates of the oscillator parameters coming from the transfer function and from the thermal noise measurement have been compared, observing a good agreement. However, in thermodynamic equilibrium, in which thermal noise can be predicted by theory, its estimate for the amplitude of oscillation was quantified lower than that expected. The same issue was found also in previous measurements.

A hypothesis is that the measuring apparatus is not correctly calibrated. As a check of this eventuality, the calibration procedure was performed with three different methods, assessing the constancy of such procedure, i.e. without observing problems. Another check was tried studying a piezoelectric actuator and then using it to provide certain sinusoidal displacements to the measuring apparatus, in order to evaluate if such displacement were correctly measured. However, the actuator showed a different behavior when it was used in the measuring apparatus with respect to before when it was independently studied, so that this calibration could not be successfully performed. Another hypothesis is that the oscillator, which we model as an isolated one to provide the theoretical prediction for thermal noise, is not really isolated. This is suggested by unexpected changes in the parameters of the transfer function of the oscillator between different measurement campaigns. In future this hypothesis will be investigated.

Appendix A

Power spectral density

The two-sided power spectral density (PSD) of a function $x(t)$ defined over all time ($t \in \mathbb{R}$) is defined as

$$S_{xx}^{(2s)}(\nu) \triangleq \lim_{T\to\infty} \frac{|\hat{x}_T(\nu)|^2}{T}, \tag{A.1}$$

where $\hat{x}_T(\nu)$ is the Fourier transform of $x(t)$ on an interval T given by

$$\hat{x}_T(\nu) \triangleq \int_{-T/2}^{T/2} x(t)e^{2\pi\nu t}dt. \tag{A.2}$$

If $x(t)$ is not defined over all $\mathbb{R}$, as it is necessary the case if $x(t)$ is a measured quantity, the Fourier transform $\hat{x}_I(\nu)$ is performed over the domain interval I and the two-sided PSD results

$$S_{xx}^{(2s)}(\nu) \triangleq \frac{|\hat{x}_I(\nu)|^2}{I}. \tag{A.3}$$

In this case the Fourier decomposition has only the components with $\nu = \frac{n}{I}$ and so the frequency resolution is $\Delta\nu = \frac{1}{I}$.

An other limitation proper to the measured quantities is that they are discrete in time. The Nyquist theorem states that a signal can be correctly reconstructed only if its frequency content is such that $f_{max} < \frac{f_s}{2}$, with f_s the sampling frequency. For the case of this thesis, $f_{max} \approx 1400$ while $f_s = 8000$, respecting the condition of the Nyquist theorem.

If $x(t)$ is real, $S_{xx}^{(2s)}(\nu) = S_{xx}^{(2s)}(-\nu)$; this allows to consider instead of a two-sided PSD a one-sided PSD, that is equal to the double of the first one but is defined only on not negative frequencies:

$$S_{xx}(\nu) \triangleq 2S_{xx}^{(2s)}(\nu), \qquad \text{with } \nu \geq 0. \tag{A.4}$$

The PSD of thermal noise is usually expressed in the one-sided form, as done in this thesis.

The PSD represents the square of the spectral content of a variable and by the Parseval's theorem is linked to the mean square of the variable:

$$\int_0^{+\infty} S_{xx}(\nu)d\nu = \langle x(t)^2 \rangle. \tag{A.5}$$

This means that the PSD indicates the contribution of the various frequencies to the variance of the variable; for the case in which $x(t)$ is the displacement of a harmonic oscillator from its equilibrium position (as in section 1.1), $\mathrm{Var}(x(t))$ is proportional to the mean energy of the oscillation and so the PSD represents the contribution of the various frequencies to such energy.

The (time) autocorrelation function of $x(t)$ (real) is defined as

$$\Gamma_x(\tau) \triangleq \langle x(t+\tau)x(t) \rangle, \tag{A.6}$$

where the angle brackets are the temporal mean over t. The Wiener-Khinchin theorem states that the two-sided PSD of $x(t)$ is equal to the Fourier trasform of the statistical average of the autocorrelation function of $x(t)$:

$$S_{xx}^{(2s)}(\nu) = \int_{-\infty}^{+\infty} \overline{\Gamma_x(\tau)} e^{2\pi\nu\tau} d\tau = \int_{-\infty}^{+\infty} \Gamma_x(\tau) e^{2\pi\nu\tau} d\tau, \tag{A.7}$$

where the last equality is valid with an ergodic process, in which the statistical average is equal to the time average.

Bibliography

[1] *The history of noise [on the 100th anniversary of its birth]* L Cohen IEEE Signal Processing Magazine 22 (6), 20-45, 2005

[2] *Thermal Agitation of Electric Charge in Conductors* H. Nyquist, Phys. Rev. 32, 110, 1 July 1928

[3] *Irreversibility and Generalized Noise* Herbert B. Callen and Theodore A. Welton, Phys. Rev. 83, 34, 1 July 1951

[4] *Zero-point thermal noise in resistors? A conclusion* Laszlo B. Kish, Metrology and Measurement Systems, 2019, vol. 26, No 1

[5] *The mathematics of Brownian motion and Johnson noise* Daniel T. Gillespie, American Journal of Physics 64, 225 (1996)

[6] *Thermal noise in mechanical experiments* Peter R. Saluson, Joint Institute for Laboratory Astrophysics, National Institute of Standards and Technology and University of Colorado, Boudler, Colorado 80309-0440 8 June 1990 Phys. Rev. D (42) (8)

[7] Charlotte Bigg, *Evident atoms: visuality in Jean Perrin's Brownian motion research*, Studies in History and Philosophy of Science Part A, Volume 39, Issue 3, 2008, Pages 312-322

[8] *Thermal Agitation of Electricity in Conductors* J. B. Johnson, Phys. Rev. 32, 97 – 1 July 1928

[9] *Measurements of the Newtonian constant of gravitation, G featured* C. Rothleitner and S. Schlamminger, Review of Scientific Instruments 88, 111101 (2017)

[10] F. Mueller, S. Heugel, and L. J. Wang, "Femto-Newton light force measurement at the thermal noise limit", Opt. Lett. 33, 539-541 (2008)

[11] *RareNoise: non-equilibrium effects in detectors of gravitational waves* L Conti et al 2010 Class. Quantum Grav. **27** 084032

[12] Tianjun Li, Felipe A. Aguilar Sandoval, Mickael Geitner, Gianpietro Cagnoli, Vincent Dolique, et al.. *Measurements of mechanical thermal noise and energy dissipation in optical dielectric coatings.* Physical Review D, American Physical Society, 2014, 89, pp.092004. 10.1103/PhysRevD.89.092004 . ensl-00922871v2

[13] *Fluctuations in nonequilibrium statistical mechanics:models, mathematical theory, physical mechanisms* R. Lamberto and C. Mejia-Monasterio, Nonlinearity, 20:(2007), pp. R1-R37.

[14] *Effects of Breaking vibrational energy euipartition on measurements of temperature in macroscopic oscillators subject to heaf flux* Livia Conti, Paolo De Gregorio, Gagik Kara- petyan, Claudia Lazzaro, Matteo Pegoraro, Michele Bonaldi and Lamberto Rondoni

[15] *Non-equilibrium "thermal noise" of low loss oscillators* G. Karapetyan, D. Agguiaro, M. Bonaldi, L. Castellani, R. Hajj, C Lazzaro, D. Mazzaro, M. Pegoraro, C. Poli, R. Thakur, L. Conti

[16] *A compact, passive setup for a low vibration noise measurements in the frequency band (300-2000) Hz* Mario Saraceni, Michele Bonaldi, Lorenzo Castellani, Livia Conti, Abdul Basheed Gounda, Stefano Longo and Matteo Pegoraro

[17] *Piezo Technology - Displacement Behavior* https://www.piceramic.com/en/expertise/piezo-technology/properties-piezo-actuators/displacement-behavior/